Noname manuscript No.
(will be inserted by the editor)

A finite difference method for earthquake sequences in poroelastic solids

Kim Torberntsson[1,2] · **Vidar Stiernström**[1,2] · **Ken Mattsson**[1] · **Eric M. Dunham**[2,3]

Received: date / Accepted: date

Abstract Induced seismicity (earthquakes caused by injection or extraction of fluids in Earth's subsurface) is a major, new hazard in the United States, the Netherlands, and other countries, with vast economic consequences if not properly managed. Addressing this problem requires development of predictive simulations of how fluid-saturated solids containing frictional faults respond to fluid injection/extraction. Here we present a finite difference method for 2D linear poroelasticity with rate-and-state friction faults, accounting for spatially variable properties. Semi-discrete stability and accuracy are proven using the summation-by-parts, simultaneous-approximation-term (SBP-SAT) framework for discretization and boundary condition enforcement. Convergence rates are verified using the method of manufactured solutions and comparison to the analytical solution to Mandel's problem. The method is then applied to study fault slip triggered by fluid injection and diffusion through high-permeability fault damage zones. We demonstrate that in response to the same, gradual forcing, fault slip can occur in either an unstable manner, as short-duration earthquakes that radiate seismic waves, or as stable, aseismic, slow slip that accumulates over much longer time scales. Finally we use these simulation results to discuss the role of frictional and elastic properties in determining the stability and nature of slip.

Keywords Poroelastic, Earthquake, Fault, Geomechanics, Porous flow, Pore pressure, Rate-and-state friction

Eric M. Dunham
E-mail: edunham@stanford.edu

[1]Department of Information Technology
Uppsala University
Uppsala, Sweden
· [2]Department of Geophysics
Stanford University, Stanford, CA, USA
· [3]Institute for Computational and Mathematical Engineering
Stanford University, Stanford, CA, USA

1 Introduction

Biot's poroelastic theory has been used extensively for civil engineering, mechanical engineering, and geophysical applications [4,34,9,49]. Applications include studies of earthen dams, ground subsidence due to fluid extraction, reservoir compaction, hydraulic fracturing, and many other geomechanical problems. More recently the theory has been used to explain earthquakes associated with fluid injection/extraction, i.e., induced seismicity [40,47,42,41], which is the specific motivation for our work. There are numerous examples of induced seismicity in recent years. A geothermal project in Basel, Switzerland, was canceled when thousands of earthquakes were triggered by water injection [7]. Reservoir compaction from gas production at the Groningen field in the Netherlands has also caused earthquakes, some large enough to cause property damage [46]. And in the past decade there has been a massive increase in earthquake rate in the central United States from disposal of wastewater co-produced with oil and gas operations in Oklahoma and nearby states [12]. Hydraulic fracturing treatments have also been linked to seismicity [3,8]. These examples show the importance of understanding induced seismicity and the processes by which fluids interact with faults to generate earthquakes. This effort requires simulations of coupled fluid flow and solid deformation in porous solids containing faults.

Finite differences, boundary elements, and finite elements have all been used to solve the linear poroelastic equations and their extensions, often referred to as the coupled fluid flow and geomechanics problem in the literature. A common approach is to couple codes for fluid flow (i.e., reservoir simulators) with separate codes for solid mechanics [31,6,19,30]. Numerical investigations are typically focused on stability and accuracy issues related to the coupling procedure. The poroelastic equations can also be solved in a single, unified code (i.e., with a fully coupled method). Stability can again be an issue, particularly for finite elements, though considerable work has led to a comprehensive understanding of the best elements and stabilization methods [50,32]. Additional work has focused on efficient solution of the coupled linear system that arises when discretizing the equations [51].

Some recent studies examine slip on faults in a poroelastic medium. Both Jha and Juanes [17] and Miah et al. [29] have taken the code coupling approach to study fault slip in reservoirs, combining reservoir simulators with the finite element mechanics code PyLith [1]. In contrast, Meng [28] uses a fully coupled finite element method to solve the poroelastic problem with fault slip. McClure and Horne [27] added rate-and-state friction in the context of a boundary element method with fluid flow and pore pressure diffusion constrained to the faults. While the previously mentioned studies have full coupling between slip, deformation, and fluid flow, another common approach is a one-way coupling procedure in which pore pressure diffusion is solved first and then used as an input to a mechanics and fault slip code [10].

In this study we present a high-order accurate and stable numerical method to solve the fully coupled linear poroelastic equations in 2D with rate-and-state frictional faults. We use finite differences, thereby allowing consideration of spatially variable material parameters. The difference operators satisfy the summation-by-parts (SBP) property and the simultaneous-approximation-term (SAT) method is used to impose boundary conditions weakly through penalty terms added to

the spatially discretized governing equations. The SBP-SAT framework facilitates analysis of stability by the energy method [44].

Sections 2-9 present the linear poroelastic equations and numerical method. Section 2 presents the linear poroelastic equations in tensor notation using two formulations, namely the pressure formulation and the fluid content formulation. In Section 3, well-posedness for the governing equations is shown in 1D using the energy method and initial boundary value problems for the two formulations are presented. Section 4 introduces the SBP operators used for the spatial discretization and for the semi-discrete stability proofs conducted in Section 5. Well-posedness for the 2D problem is proven in Section 6, which also presents initial boundary value problems in the two formulations. The SBP operators are extended to 2D and to systems of equations in Section 7. Semi-discrete stability for the linear poroelastic equations in 2D is shown in Section 8 using the SBP-SAT discretization and the energy method. Time-stepping procedures are described in Section 9. Convergence tests are performed, first using the method of manufactured solutions (Section 10) and then for the classic Mandel's problem (Section 11). The method is extended to handle frictional faults in Section 12. Rate-and-state friction and an adaptive time-stepping procedure are presented, followed by simulations illustrating fault slip triggered by fluid injection.

2 Governing equations

In this section, two equivalent formulations of the linear poroelastic equations are introduced. In the *pressure formulation*, the unknown fields are the displacements u_i and the pore pressure p. The *fluid content formulation* solves for u_i and p', the deviation of pressure from its undrained response. The fluid content formulation offers several computational advantages, especially for poroelastic problems involving frictional fault dynamics.

2.1 Pressure formulation

We proceed by reviewing the linear, isotropic poroelastic equations. The material parameters can be spatially variable, but are independent of time. The total stress σ_{ij} is obtained from Hooke's law,

$$\sigma_{ij} = 2G\epsilon_{ij} + \left(K - \frac{2}{3}G\right)\epsilon_{kk}\delta_{ij} - \alpha p\delta_{ij}, \tag{1}$$

where

$$\epsilon_{ij} = \frac{1}{2}\left(\frac{\partial u_i}{\partial x_j} + \frac{\partial u_j}{\partial x_i}\right), \tag{2}$$

are the strains, δ_{ij} is the Kronecker delta, $G \geq 0$ is the shear modulus, $K \geq 0$ is the drained bulk modulus, and $0 \leq \alpha \leq 1$ is Biot's coefficient. A quasi-static approximation to the momentum balance is used,

$$\frac{\partial \sigma_{ij}}{\partial x_j} = 0, \tag{3}$$

where body forces such as gravity are neglected. Combining Eqs. 1–3 yields the mechanical equilibrium equation,

$$\frac{\partial}{\partial x_j}\left[\left(K+\frac{G}{3}\right)\frac{\partial u_j}{\partial x_i}\right]+\frac{\partial}{\partial x_j}\left(G\frac{\partial u_i}{\partial x_j}\right)=\frac{\partial(\alpha p)}{\partial x_i}. \tag{4}$$

From Darcy's law, conservation of fluid mass, and thermodynamic considerations, the fluid diffusion equation is obtained,

$$M^{-1}\frac{\partial p}{\partial t}-\frac{\partial}{\partial x_i}\left(\kappa\frac{\partial p}{\partial x_i}\right)=-\alpha\frac{\partial^2 u_k}{\partial x_k \partial t}, \tag{5}$$

where $M \geq 0$ is Biot's modulus (the reciprocal of a storage coefficient) and $\kappa \geq 0$ is the mobility (permeability divided by fluid viscosity). Together Eqs. 4 and 5 constitute the linear poroelastic equations. We refer to this form of the equations, written in terms of displacement u_i and pressure p, as the pressure formulation.

2.2 Fluid content formulation

The pressure formulation of the linear poroelastic equations presented in Section 2.1 can be solved using either explicit or implicit time integration methods. However there is little to be gained from an explicit method because Eq. 5 has two terms with partial time derivatives of both u_i and p. Thus either time discretization method requires a linear system solve for both u_i and p simultaneously. However, as explained in Section 12, problems involving frictional fault dynamics can be more efficiently solved with an explicit time integration method for fluid diffusion and a linear system solve for only u_i in the mechanics problem. This is because time scales characterizing frictional dynamics are generally less than those governing fluid diffusion. We therefore seek an alternative formulation of the problem that is suitable for explicit time integration.

To do this, we rewrite the governing equations in terms of perturbations about the undrained response of the system, i.e., the response at sufficiently short time scales that fluid flow can be neglected [4,34,9,49]. We introduce the undrained bulk modulus, $K_u = K+\alpha^2 M$, and the variation of fluid content ζ. An expression for the undrained pore pressure p_u is obtained by setting the diffusive term in Eq. 5 to zero and integrating in time, resulting in

$$p_u = -M\alpha\frac{\partial u_k}{\partial x_k}. \tag{6}$$

The relation between the pore pressure p, the undrained pore pressure p_u, and the variation of fluid content ζ is $p = M\zeta + p_u$. We now introduce the field variable p', referred to as the deviation from the undrained pore pressure, defined as

$$p' = M\zeta = p + M\alpha\frac{\partial u_k}{\partial x_k}. \tag{7}$$

Note that the relation between the variation of fluid content ζ and the deviation from the undrained pore pressure p' is a relation between differential changes, meaning that even for a spatially variable M, $\partial p'/\partial x_i = M\partial\zeta/\partial x_i$. To derive the

governing equation for p', Eqs. 6 and 7 are inserted into Eq. 5, resulting in an uncoupled homogeneous diffusion equation,

$$M^{-1}\frac{\partial p'}{\partial t} - \frac{\partial}{\partial x_i}\left(\kappa\frac{\partial p'}{\partial x_i}\right) = 0, \tag{8}$$

which is suitable for explicit time integration.

In addition, the mechanical equilibrium equations must be stated in terms of p' instead of p. Inserting Eq. 7 into Eq. 4 and using the definition of K_u yields

$$\frac{\partial}{\partial x_j}\left[\left(K_u + \frac{G}{3}\right)\frac{\partial u_j}{\partial x_i}\right] + \frac{\partial}{\partial x_j}\left(G\frac{\partial u_i}{\partial x_j}\right) = \frac{\partial(\alpha p')}{\partial x_i}. \tag{9}$$

The left-hand side of Eq. 9 is simply the usual linear elastic mechanics operator, but with undrained elastic moduli. With Eqs. 8 and 9 we have derived an alternative formulation of the linear poroelastic equations, henceforth referred to as the fluid content formulation. The unknown fields are $\{u_i, p'\}$ with material parameters $\{K_u, G, \alpha, M, \kappa\}$, compared to the unknown fields $\{u_i, p\}$ with material parameters $\{K, G, \alpha, M, \kappa\}$ in the pressure formulation. In certain sections, alternative material parameters are used; see [34,9,49] for discussion of poroelastic parameter sets. Parameters used later include the drained and undrained Lamé's first modulus, $\lambda = K - 2G/3$ and $\lambda_u = K_u - 2G/3$; the drained and undrained Poisson's ratio, $\nu = (3K - 2G)/2(3K + G)$ and $\nu_u = (3K_u - 2G)/2(3K_u + G)$; Skempton's coefficient, $B = (K_u - K)/\alpha K_u$; and the hydraulic diffusivity, $c = \kappa M$.

3 Energy balance and well-posedness in 1D

This section presents the initial boundary value problems for the two formulations of the linear poroelastic equations and establishes well-posedness using the energy method. We begin in 1D and later generalize to 2D. While the following results are all well known, they are summarized here since the same steps are followed when proving stability of the semi-discrete method.

3.1 Initial boundary value problem for the pressure formulation

Let the domain be defined as $\Omega = \{x : 0 \le x \le 1\}$ and let the displacement u and the pore pressure p be continuous and real valued functions on Ω. The 1D versions of Eqs. 4 and 5 are

$$0 = (E'u_x)_x - (\alpha p)_x, \quad 0 \le x \le 1, \quad t \ge 0, \tag{10}$$

$$M^{-1}p_t = (\kappa p_x)_x - \alpha u_{xt}, \quad 0 \le x \le 1, \quad t \ge 0, \tag{11}$$

where $E' = K + 4G/3$ and subscripts indicate partial derivatives (e.g., $u_x = \partial u/\partial x$). The initial conditions are $u = h_1(x)$, $p = h_2(x)$, $0 \le x \le 1$, $t = 0$.

Boundary conditions for the mechanical equilibrium equation can be placed on either displacement u (Dirichlet condition) or traction $\sigma = E'u_x - \alpha p$ (Neumann condition), and for the fluid diffusion equation on either pore pressure p (Dirichlet condition) or discharge velocity $q = -\kappa p_x$ (Neumann condition). One way to perform a well-posedness analysis on both the Neumann and Dirichlet conditions

at the same time is to use Robin conditions, in which a linear combination of Dirichlet and Neumann conditions is imposed:

$$\gamma_0 u - \sigma = g_0, \quad \delta_0 p + q = f_0, \quad x = 0, \quad t \geq 0, \tag{12}$$

$$\gamma_1 u + \sigma = g_1, \quad \delta_1 p - q = f_1, \quad x = 1, \quad t \geq 0, \tag{13}$$

where $\gamma_0, \gamma_1, \delta_0, \delta_1 \geq 0$. The Robin conditions impose Neumann conditions when $\gamma, \delta = 0$ and Dirichlet conditions in the limit $\gamma, \delta \to \infty$.

Remark 1 The Robin BC in Eqs. 12 and 13 is not the most obvious way of imposing Dirichlet BC. The reason for introducing this is that it will simplify the discrete analysis. We will discuss this further in the semi-discrete analysis.

Since the Dirichlet conditions are imposed using the penalty terms γ, δ, the boundary data must scaled differently when imposing Dirichlet conditions compared to imposing Neumann conditions:

$$g_0 = \begin{cases} \gamma_0 g_0^D \\ -g_0^N, \end{cases}, g_1 = \begin{cases} \gamma_1 g_1^D \\ g_1^N, \end{cases}, f_0 = \begin{cases} \delta_0 f_0^D \\ f_0^N, \end{cases}, f_1 = \begin{cases} \delta_1 f_1^D \\ -f_1^N \end{cases}, \tag{14}$$

where g^D, f^D indicate Dirichlet data and g^N, f^N indicate Neumann data.

The inner product and the A-norm, which will be used extensively in the coming analysis, is defined as follows:

Definition 1 Let $u \in l^2\Omega$ be a real-valued vector function $u = [u^{(1)}, u^{(2)}, \ldots..., u^{(k)}]^T$ with k components and let A be a symmetric positive semi-definite matrix, i.e., $A = A^T \geq 0$. The inner product for $u, v \in l^2\Omega$ is defined as $(u, Av) = \int_\Omega u^T Av d\Omega$ and the A-norm is defined via $\|u\|_A^2 = (u, Au) = \int_\Omega u^T Au d\Omega$.

An energy estimate (i.e., mechanical energy balance) for the linear poroelastic equations is derived by multiplying Eq. 10 with u_t and Eq. 11 with p, integrating over Ω, and using integration by parts to obtain

$$\frac{d}{dt}\left(\|u_x\|_{E'}^2 + \|p\|_{M^{-1}}^2\right) = -2\|p_x\|_\kappa^2 + 2(u_t\sigma - pq)|_0^1, \tag{15}$$

where the terms within the temporal derivative on the left-hand side defines the energy of the system and the right-hand side its time evolution. Imposing homogeneous Dirichlet or Neumann conditions eliminates the boundary work rate terms to yield

$$\frac{d}{dt}\left(\|u_x\|_{E'}^2 + \|p\|_{M^{-1}}^2\right) = -2\|p_x\|_\kappa^2. \tag{16}$$

Hence, the linear poroelastic equations given by Eq. 10 and 11 are well-posed for the BC in Eqs. 12 and 13.

The energy estimate for Neumann and Dirichlet BC imposed with the Robin technique (Eqs. 12 and 13) is equal to Eq. 16 in the two limits $\gamma, \delta \to \infty$ and $\gamma, \delta = 0$. For Neumann conditions this is trivial, since the conditions are imposed in the same way as standard Neumann, but for Dirichlet conditions this is not as simple to show. In Eq. 15 one can either substitute σ and q or u and p (or any combination) at the boundaries using Eqs. 12 and 13. When substituting σ and q the energy estimate is

$$\frac{d}{dt}\left(\|u_x\|_{E'}^2 + \|p\|_{M^{-1}}^2 + \gamma_1 u^2|_1 + \gamma_0 u^2|_0\right) = -2\|p_x\|_\kappa^2 - 2\delta_1 p^2|_1 - 2\delta_0 p^2|_0, \tag{17}$$

which also is a well-posed energy estimate for $\gamma, \delta > 0$. It is not immediately clear that the Robin energy estimate (Eq. 17) converges to the Dirichlet energy estimate (Eq. 16) as $\gamma, \delta \to \infty$. However, if u and p are substituted at the boundaries in Eq. 15 using Eqs. 12 and 13, we obtain an energy estimate that is equivalent to Eq. 17, but now expressed in terms of σ and κp_x:

$$\frac{d}{dt}\left(\|u_x\|^2_{E'} + \|p\|^2_{M^{-1}} + \frac{1}{\gamma_1}\sigma^2\Big|_1 + \frac{1}{\gamma_0}\sigma^2\Big|_0 \right) = -2\|p_x\|^2_\kappa - 2\frac{(q)^2}{\delta_1}\Big|_1 - 2\frac{(q)^2}{\delta_0}\Big|_0, \quad (18)$$

which is a well-posed energy estimate for $\gamma, \delta > 0$. It is also clear that the energy estimate in Eq. 18 is equal to the energy estimate in Eq. 16 in the limit $\gamma, \delta \to \infty$. Since the energy estimates in Eqs. 17 and 18 are equivalent, Eq. 17 is equal to the energy estimate in Eq. 18 in the limit $\gamma, \delta \to \infty$. This result is of importance for showing that the Robin boundary conditions approximate the Dirichlet conditions in the limit $\gamma, \delta \to \infty$ also in the semi-discrete case.

3.2 Initial-boundary value problem for the fluid content formulation

The 1D version of the fluid content formulation introduced in Section 2.2 is derived from the 1D pressure formulation problem (Eqs. 10–13) using the following relation:

$$p = p' + p_u = p' - M\alpha u_x. \quad (19)$$

Since the two formulations are equivalent, well-posedness is already established. However, both the boundary and initial conditions should be stated in terms of u and p'. Inserting Eq. 19 into Eqs. 10–13 results in an initial-boundary value problem for the fluid content formulation:

$$0 = (E'_u u_x)_x - (\alpha p')_x, \quad 0 \le x \le 1, \quad t \ge 0, \quad (20)$$

$$M^{-1} p'_t = (\kappa p'_x)_x, \quad 0 \le x \le 1, \quad t \ge 0, \quad (21)$$

with initial conditions $u = h_1(x)$, $p' = h_2(x) + M\alpha dh_1/dx$, $0 \le x \le 1$, $t = 0$, and boundary conditions identical to Eqs. 12 and 13 except that $\sigma = E'_u u - \alpha p'$, $p = p' - M\alpha u_x$, and $q = -\kappa(p' - M\alpha u_x)_x$, where $E'_u = K_u + 4G/3$.

4 SBP finite differences in 1D

To explain the SBP-SAT finite difference method, some definitions are needed. SBP operators [43,25,23] are essentially central finite difference stencils, closed at the boundaries with a careful choice of one-sided difference stencils, that mimic the underlying integration-by-parts formula in a discrete norm. In the present paper the SBP operators are addressed by the accuracy of the interior finite difference stencil (the boundary accuracy is generally smaller).

The domain Ω is discretized using m grid points,

$$x_i = (i-1)\Delta x, \quad i = 1, 2, \ldots, m, \quad \Delta x = \frac{1}{m-1}. \quad (22)$$

Let p and u be discrete column vectors with m components that approximate their continuous counterparts at the grid points x_i, i.e., $p = [p_1, p_2, \ldots, p_m]^T$. The discrete inner product and norm are defined as follows:

Definition 2 Let $u, v \in \mathbf{R}^m$ be discrete real-valued solution vectors and let A be a symmetric positive semi-definite matrix, i.e., $A = A^T \geq 0$ and H be diagonal and positive definite. The discrete inner product is defined as $(u, HAv) = u^T HAv$ and the corresponding norm is defined via $\|u\|^2_{HA} = (u, HAu) = u^T HAu$.

The following vectors will be frequently used in the SAT penalty treatment: $e_1 = [1, 0, 0, \ldots, 0]$, $e_m = [0, 0, \ldots, 0, 1]$. Let $B = -e_1 e_1^T + e_m e_m^T$, and A a matrix with the variable coefficients $a(x)$ injected on the diagonal, i.e., $A = \text{diag}(a_1, \ldots, a_m)$.

The following three definitions, previously introduced in [23], are important to the present study:

Definition 3 An explicit pth-order accurate finite difference scheme with minimal stencil width of a Cauchy problem is denoted a pth-order accurate narrow-stencil.

Definition 4 A difference operator $D_1 = H^{-1}(Q+B)$ approximating $\partial/\partial x$, using a pth-order accurate narrow-stencil, is said to be a pth-order accurate narrow-diagonal first-derivative SBP operator if H is diagonal and positive definite and $Q + Q^T = 0$.

Definition 5 Let $D_2^{(a)} = H^{-1}(-M^{(a)} + BAS)$ approximate $\frac{\partial}{\partial x}\left(a\frac{\partial}{\partial x}\right)$, where $a(x) > 0$ is a smooth function, using pth-order accurate narrow-stencil. $D_2^{(a)}$ is said to be a pth-order accurate narrow-diagonal second derivative SBP operator, if H is diagonal and positive definite, M is symmetric and positive semi-definite, and S approximates the first derivative at the boundaries.

Note that in order to obtain energy estimates for schemes using both D_1 and $D_2^{(a)}$ the norm H has to be identical for the two operators. It was shown in [26] that for problems with a combination of mixed $(\partial^2/\partial x \partial y)$ and non-mixed $(\partial^2/\partial x^2, \partial^2/\partial y^2)$ second order derivatives, stability is not guaranteed from Definition 5 alone. An important relationship between the first order and second order narrow SBP operators called compatibility was introduced in [26], where it was shown that for problems with both mixed and non-mixed derivatives, compatible operators are required in order for stability proofs to be obtained. The following definition of compatibility was first stated in [23]:

Definition 6 Let D_1 and $D_2^{(a)}$ be pth-order accurate narrow-diagonal first- and second-derivative SBP operators. If $M^{(a)} = D_1^T HAD_1 + R^{(a)}$, and the remainder $R^{(a)}$ is symmetric positive semi-definite, D_1 and $D_2^{(a)}$ are called compatible.

The remainder term $R^{(a)}$ is essentially a linear combination of higher order derivatives (see [23] for details).

5 Semi-discrete stability in 1D

In this section we use the SBP-SAT procedure to spatially discretize the 1D initial-boundary value problems stated in Section 3 and prove stability of the semi-discrete problem.

We begin with the pressure formulation. Using fully compatible SBP operators (Section 4), Eqs. 10 and 11 are discretized with the boundary conditions (Eqs. 12 and 13) imposed using the SAT technique:

$$0 = D_2^{(E')}u - D_1\alpha p + SAT_1, \quad t \geq 0, \tag{23}$$

$$M^{-1}p_t = D_2^{(\kappa)}p - \alpha D_1 u_t + SAT_2, \quad t \geq 0, \tag{24}$$

with initial conditions $u = h_1$, $p = h_2$, $t = 0$, where material parameters are stored as diagonal matrices (e.g., $E' = \text{diag}(E'_1, E'_2, \ldots, E'_m)$), and

$$SAT_1 = H^{-1}e_1(e_1^T(-\gamma_0 u + \sigma) + g_0) + H^{-1}e_m(e_m^T(-\gamma_1 u - \sigma) + g_1), \tag{25}$$

$$SAT_2 = H^{-1}e_1(e_1^T(-\delta_0 p - q) + f_0) + H^{-1}e_m(e_m^T(-\delta_1 p + q) + f_1), \tag{26}$$

where $\sigma = E'D_1u - \alpha p$ and $q = -\kappa D_1 p$. The boundary data are set analogously to the continuous case in Eq. 14.

Using the SBP-SAT method, semi-discrete stability can be proven using the semi-discrete version of the continuous energy method introduced in Section 3. Analogous to the procedure in the continuous case, the semi-discrete energy method consists of multiplying the mechanical equilibrium equation (Eq. 23) by $u_t^T H$ and adding the transpose, and multiplying the fluid diffusion equation (Eq. 24) by $p^T H$ and adding the transpose, resulting in the semi-discrete version of the continuous energy estimate (Eq. 17):

$$\frac{d}{dt}\left(\|D_1u\|^2_{HE'} + \|p\|^2_{HM^{-1}} + \|u\|^2_{R^{(E')}} + \gamma_1 u_m^2 + \gamma_0 u_1^2\right) = \\ -2\|D_1 p\|^2_{H\kappa} - 2\|p\|^2_{R^{(\kappa)}} - 2\delta_1 p_m^2 - 2\delta_0 p_1^2, \tag{27}$$

where Definitions 4–6 and $Q + Q^T = 0$ were used. Note that the energy estimate is well-posed for $\gamma, \delta \geq 0$. For Neumann boundary conditions ($\gamma, \delta = 0$), Eq. 27 reduces to

$$\frac{d}{dt}\left(\|D_1u\|^2_{HE'} + \|p\|^2_{HM^{-1}} + \|u\|^2_{R^{(E')}}\right) = -2\|D_1 p\|^2_{H\kappa} - 2\|p\|^2_{R^{(\kappa)}}, \tag{28}$$

which is the semi-discrete version of Eq. 16.

At this point we have developed a stable difference method for solving the pressure formulation. Now we extend the method to the fluid content formulation (Section 2.2). The undrained pressure in the continuous case is defined in Eq. 6 and its discrete counterpart in 1D is

$$p_u = -M\alpha D_1 u. \tag{29}$$

The semi-discrete version of the fluid content formulation in one spatial dimension, discretized using the SBP-SAT method, is

$$0 = D_2^{(E'_u)}u + H^{-1}R^{(M\alpha^2)}u - D_1\alpha p' + SAT_1, \quad t \geq 0, \tag{30}$$

$$M^{-1}p'_t = D_2^{(\kappa)}p' - D_2^{(\kappa)}M\alpha D_1 u + SAT_2, \quad t \geq 0, \tag{31}$$

with initial conditions $u = h_1$, $p' = h_2 + M\alpha D_1 h_1$, $t = 0$, where

$$SAT_1 = H^{-1}e_1(e_1^T(-\gamma_0 u + \sigma) + g_0) + H^{-1}e_m(e_m^T(-\gamma_1 u - \sigma) + g_1), \tag{32}$$

$$SAT_2 = H^{-1}e_1(e_1^T(-\delta_0 p - q) + f_0) + H^{-1}e_m(e_m^T(-\delta_1 p + q) + f_1). \tag{33}$$

The SAT terms in Eqs. 32 and 33 are identical to the SAT terms in Eqs. 25 and 26, but expressed in terms of u and p' via the relations $\sigma = E'_u D_1 u - \alpha p'$, $p = p' - M\alpha D_1 u$ and $q = -\kappa D_1(p' - M\alpha D_1 u)$. Note that the interior penalty terms, $H^{-1}R^{(M\alpha^2)}u$ and $-D_2^{(\kappa)}\alpha M D_1 u$, appearing in Eqs. 30 and 31, arise as a consequence of the change of variable from p to p'; for more details, see [45].

It can be shown [45] that Eqs. 31 and 24 are identical, establishing equivalence of the pressure and fluid content formulations in the semi-discrete case.

6 Energy balance and well-posedness in 2D

In this section, the initial-boundary value problems for the two formulations of the linear poroelastic equations for 2D plane strain are presented. The energy method is then used to show well-posedness in a similar fashion to the procedure presented in Section 3.

6.1 Initial-boundary value problem for the pressure formulation

Let the 2D domain Ω be a rectangle with sides of length L_x and L_y in the x- and y-directions, respectively, i.e., $\Omega = \{(x, y) : 0 \le x \le L_x, 0 \le y \le L_y\}$. The west boundary is $\partial\Omega_W = \{(x, y) : x = 0, 0 \le y \le L_y\}$, with similar notation for the other (east, south, and north) boundaries. For the 2D plane strain problem, denoting $u_1 = u$, and $u_2 = v$ and introducing $\lambda = K - 2G/3$, the linear poroelastic equations (Eqs. 4 and 5) are

$$\left((\lambda + 2G)\, u_x + \lambda v_y\right)_x + \left(G u_y + G v_x\right)_y = (\alpha p)_x\,, \quad (x, y) \in \Omega, \quad t \ge 0 \tag{34}$$

$$\left(G u_y + G v_x\right)_x + \left(\lambda u_x + (\lambda + 2G)\, v_y\right)_y = (\alpha p)_y\,, \quad (x, y) \in \Omega, \quad t \ge 0 \tag{35}$$

$$M^{-1} p_t = (\kappa p_x)_x + (\kappa p_y)_y - \alpha\left(u_{xt} + v_{yt}\right), \quad (x, y) \in \Omega, \quad t \ge 0. \tag{36}$$

and the stress tensor is

$$\sigma = \begin{bmatrix} \sigma_{xx} & \sigma_{xy} \\ \sigma_{xy} & \sigma_{yy} \end{bmatrix} = \begin{bmatrix} (\lambda + 2G)\, u_x + \lambda v_y - \alpha p & G(u_y + v_x) \\ G(u_y + v_x) & (\lambda + 2G)\, v_y + \lambda u_x - \alpha p \end{bmatrix}. \tag{37}$$

Rewriting Eqs. 34–36 using vector notation results in the initial-boundary value problem in the pressure formulation:

$$0 = (\mathbf{A}\mathbf{u}_x + \mathbf{C}\mathbf{u}_y)_x + (\mathbf{B}\mathbf{u}_y + \mathbf{C}^T\mathbf{u}_x)_y - \nabla(\alpha p), \quad (x, y) \in \Omega, \quad t \ge 0, \tag{38}$$

$$M^{-1} p_t = (\kappa p_x)_x + (\kappa p_y)_y - \alpha\left(u_{xt} + v_{yt}\right), \quad (x, y) \in \Omega, \quad t \ge 0, \tag{39}$$

where $\mathbf{u} = [u \quad v]^T$ and

$$\mathbf{A} = \begin{bmatrix} \lambda + 2G & 0 \\ 0 & G \end{bmatrix}, \quad \mathbf{B} = \begin{bmatrix} G & 0 \\ 0 & \lambda + 2G \end{bmatrix}, \quad \mathbf{C} = \begin{bmatrix} 0 & \lambda \\ G & 0 \end{bmatrix}. \tag{40}$$

The initial conditions are $\mathbf{u} = \mathbf{h}_1(x, y)$, $p = h_2(x, y)$, $(x, y) \in \Omega$, $t = 0$, where $\mathbf{h}_1$ is a two-component vector specifying the initial conditions for u and v, respectively. The Robin boundary conditions are

$$\boldsymbol{\gamma}_W \mathbf{u} - \mathbf{T}_x = \mathbf{g}_W, \;\; \delta_W p + q_x = f_W, \;\; (x, y) \in \partial\Omega_W, \quad t \ge 0, \tag{41}$$

for the west boundary (and similarly for other boundaries), where $\boldsymbol{\gamma} = \text{diag}(\gamma_1, \gamma_2)$ at each boundary, where γ_1 and γ_2 are the penalties for the first and second mechanical equilibrium equations, respectively, and δ is a scalar penalty for the fluid diffusion equation, as in the 1D case. The vectors $\mathbf{T}_x$ and $\mathbf{T}_y$ are defined as the traction vectors for surfaces with unit normals in the positive x and y directions, respectively, namely

$$\mathbf{T}_x = [\sigma_{xx} \quad \sigma_{xy}]^T = \mathbf{A}\mathbf{u}_x + \mathbf{C}\mathbf{u}_y - \alpha p \hat{x}, \tag{42}$$

$$\mathbf{T}_y = [\sigma_{xy} \quad \sigma_{yy}]^T = \mathbf{B}\mathbf{u}_y + \mathbf{C}^T\mathbf{u}_x - \alpha p \hat{y}, \tag{43}$$

where $\hat{x} = [1 \quad 0]^T$ and $\hat{y} = [0 \quad 1]^T$. The fluid discharge velocities in the x and y directions are defined as $q_x = -\kappa p_x$ and $q_y = -\kappa p_y$, respectively. The boundary data vectors $\mathbf{g}$ are two-component vectors with boundary data for u and v, respectively. Similarly to the 1D case, the boundary data are constructed as

$$\mathbf{g}_W = \begin{cases} \boldsymbol{\gamma}_W \mathbf{g}_W^D \\ -\mathbf{g}_W^N \end{cases}, \quad f_W = \begin{cases} \delta_W f_W^D \\ f_W^N \end{cases}, \tag{44}$$

for the west boundary (and similarly for other boundaries), where $\mathbf{g}^D$, f^D indicate Dirichlet data and $\mathbf{g}^N$, f^N indicate Neumann data.

6.2 Well-posedness

Well-posedness of the initial-boundary value problem presented in equations Eqs. 38–41 is shown using the energy method, as in the 1D case. Multiply Eqs. 38 and 36 with $\mathbf{u}_t^T$ and p^T, respectively, and integrate by parts, to yield

$$\frac{d}{dt}\|\hat{\mathbf{u}}\|_{\mathbf{P}}^2 = -(\mathbf{u}_t, \nabla(\alpha p)) - (\nabla(\alpha p), \mathbf{u}_t) + 2BT_1, \tag{45}$$

$$\frac{d}{dt}\|p\|_{M^{-1}}^2 = -2\|p_x\|_\kappa^2 - 2\|p_y\|_\kappa^2 + (\mathbf{u}_t, \nabla(\alpha p)) + (\nabla(\alpha p), \mathbf{u}_t) + 2BT_2, \tag{46}$$

where $\hat{\mathbf{u}} = [\mathbf{u}_x \quad \mathbf{u}_y]^T$ and

$$\mathbf{P} = \begin{bmatrix} \mathbf{A} & \mathbf{C} \\ \mathbf{C}^T & \mathbf{B} \end{bmatrix} = \begin{bmatrix} \lambda + 2G & 0 & 0 & \lambda \\ 0 & G & G & 0 \\ 0 & G & G & 0 \\ \lambda & 0 & 0 & \lambda + 2G \end{bmatrix}. \tag{47}$$

Both $\|\hat{\mathbf{u}}\|_{\mathbf{P}}^2$ and $\|p\|_{M^{-1}}^2$ are obtained using Definition 1. Note that all the elements of $\mathbf{P}$ are positive since $K \geq 0$, $G \geq 0$ and $\lambda + 2G = K + 4G/3 \geq 0$. Furthermore $\mathbf{P}$ is diagonally dominant, and therefore also positive semi-definite and hence $\|\hat{\mathbf{u}}\|_{\mathbf{P}}^2$ is a valid norm.

The terms BT_1 and BT_2 in Eqs. 45 and 46 are boundary terms obtained when integrating by parts:

$$BT_1 = \int_0^{L_y} \mathbf{u}_t^T(\mathbf{A}\mathbf{u}_x + \mathbf{C}\mathbf{u}_y)\Big|_{x=0}^{x=L_x} dy + \int_0^{L_x} \mathbf{u}_t^T(\mathbf{B}\mathbf{u}_y + \mathbf{C}^\mathbf{T}\mathbf{u}_x)\Big|_{y=0}^{y=L_y} dx, \tag{48}$$

$$BT_2 = -\int_0^{L_y} \alpha p u_t + p q_x\Big|_{x=0}^{x=L_x} dy - \int_0^{L_x} \alpha p v_t + p q_y\Big|_{y=0}^{y=L_y} dx. \tag{49}$$

An energy estimate for the system is then obtained by adding Eqs. 45 and 46:

$$\frac{d}{dt}\left(\|\hat{\mathbf{u}}\|_P^2 + \|p\|_{M^{-1}}^2\right) = -2\|p_x\|_\kappa^2 - 2\|p_y\|_\kappa^2 + 2BT, \tag{50}$$

where

$$BT = \int_0^{L_y} \mathbf{u}_t^T \mathbf{T}_x - pq_x\Big|_{x=0}^{x=L_x} dy + \int_0^{L_x} \mathbf{u}_t^T \mathbf{T}_y - pq_y\Big|_{y=0}^{y=L_y} dx. \tag{51}$$

Inserting the boundary conditions (Eq. 41) with homogeneous data yields

$$\frac{d}{dt}E = -2\|p_x\|_\kappa^2 - 2\|p_y\|_\kappa^2 + 2\tilde{BT}, \tag{52}$$

where

$$\begin{aligned} E = \|\hat{\mathbf{u}}\|_P^2 + \|p\|_{M^{-1}}^2 + \int_0^{L_y} \|\mathbf{u}\|_{\boldsymbol{\gamma}_W}^2\Big|^{x=0} dy + \int_0^{L_y} \|\mathbf{u}\|_{\boldsymbol{\gamma}_E}^2\Big|^{x=L_x} dy \\ + \int_0^{L_x} \|\mathbf{u}\|_{\boldsymbol{\gamma}_S}^2\Big|^{y=0} dx + \int_0^{L_x} \|\mathbf{u}\|_{\boldsymbol{\gamma}_N}^2\Big|^{y=L_y} dx, \end{aligned} \tag{53}$$

and

$$\tilde{BT} = -\delta_W \int_0^{L_y} p^2\Big|^{x=0} dy - \delta_E \int_0^{L_y} p^2\Big|^{x=L_x} dy - \delta_S \int_0^{L_x} p^2\Big|^{y=0} dx - \delta_N \int_0^{L_x} p^2\Big|^{y=L_y} dx. \tag{54}$$

The energy E is positive for $\boldsymbol{\gamma} \geq 0$ and furthermore $dE/dt \leq 0$ for $\delta \geq 0$. Thus, for $\boldsymbol{\gamma} \geq 0$ and $\delta \geq 0$, Eq. 41 is a well-posed set of boundary conditions and we have shown well-posedness of the initial-boundary value problem presented in Eqs. 38–41.

In the 1D analysis presented in Section 3, it was shown that the energy estimate obtained using the Robin technique is equal to the energy estimates for Neumann conditions, when γ, $\delta = 0$, and Dirichlet conditions in the limit γ, $\delta \to \infty$. This result holds also in the 2D case, and can be shown using the same procedure as in the 1D analysis.

6.3 Initial-boundary value problem for the fluid content formulation

This section presents the initial-boundary value problem for the fluid content formulation in 2D. Well-posedness of the initial-boundary value problem follows directly from equivalence of the fluid content and pressure formulations. However, the problem should be expressed in terms of $\mathbf{u}$ and p', rather than $\mathbf{u}$ and p. In 2D, the relationship between p, $\mathbf{u}$, and p' is

$$p = p' - M\alpha\nabla\cdot\mathbf{u}. \tag{55}$$

Using Eq. 55 to reformulate Eqs. 38 and 39 results in

$$0 = (\mathbf{A}_u\mathbf{u}_x + \mathbf{C}_u\mathbf{u}_y)_x + (\mathbf{B}_u\mathbf{u}_y + \mathbf{C}_u^T\mathbf{u}_x)_y - \nabla(\alpha p'), \quad (x,y) \in \Omega, \quad t \geq 0, \tag{56}$$

$$M^{-1}p'_t = \left(\kappa p'_x\right)_x + \left(\kappa p'_y\right)_y, \quad (x,y) \in \Omega, \quad t \geq 0, \tag{57}$$

with initial conditions $\mathbf{u} = \mathbf{h}_1(x,y)$, $p' = h_2(x,y) + M\alpha\nabla\cdot\mathbf{h}_1(x,y)$, $(x,y)\in\Omega$, $t=0$, and boundary conditions

$$\boldsymbol{\gamma}_W\mathbf{u} - \mathbf{T}_x = \mathbf{g}_W, \quad \delta_W p + q_x = f_W, \ (x,y)\in\partial\Omega_W, \quad t\geq 0, \tag{58}$$

for the west side (and similarly for other sides). Here the matrices A_u, B_u, and C_u in Eq. 56 are constructed in the same way as in Eq. 40 with λ replaced by the first Lamé parameter under undrained loading, $\lambda_u = \lambda + \alpha^2 M$. The tractions and discharge velocities are defined as

$$\mathbf{T}_x = \mathbf{A_u}\mathbf{u}_x + \mathbf{C_u}\mathbf{u}_y - \alpha p'\hat{x}, \quad \mathbf{T}_y = \mathbf{B_u}\mathbf{u}_y + \mathbf{C_u}^T\mathbf{u}_x - \alpha p'\hat{y}, \tag{59}$$

$$q_x = -\kappa(p' - M\alpha\nabla\cdot\mathbf{u})_x, \quad q_y = -\kappa(p' - M\alpha\nabla\cdot\mathbf{u})_y. \tag{60}$$

The boundary data are set as in Eq. 44.

7 SBP finite differences in 2D

Before commencing with a semi-discretization and stability analysis of the 2D problem, we explain how the operators presented in Section 4 can be extended to 2D and systems of equations. Let the domain $\Omega = \{(x,y) : 0\leq x\leq L_x, 0\leq y\leq Ly\}$ be discretized on an $N_x\times N_y$ equidistant grid defined as

$$\begin{aligned} x_i &= (i-1)\Delta x,\ i = 1,2,\ldots,N_x,\ \Delta x = L_x/(N_x-1),\\ y_j &= (j-1)\Delta y,\ j = 1,2,\ldots,N_y,\ \Delta y = L_y/(N_y-1). \end{aligned} \tag{61}$$

A function $u = u(x,y)$ defined on Ω is discretized as a length N_xN_y vector w. One can think of w as a "vector of vectors," where the element $u(x_i,y_j)$ is located at $w_{N_y i+j}$. The extension of operators to multiple dimensions and systems of equations can be realized using the Kronecker product defined as:

Definition 7 Let A and B be matrices of dimensions $p\times q$ and $m\times n$, respectively. The Kronecker product of A with B is defined as

$$A\otimes B = \begin{bmatrix} a_{1,1}B & \ldots & a_{1,q}B \\ \vdots & \ddots & \vdots \\ a_{p,1}B & \ldots & a_{p,q}B \end{bmatrix}. \tag{62}$$

Utilizing how the values of the 2D vector v are stored, the Kronecker product (Eq. 62) can be used to construct 2D operators from the 1D operators. The following operators are used to discretize the 2D linear poroelastic equations:

$$D_{1x} = D_1\otimes I_{N_y}, \quad D_{1y} = I_{N_x}\otimes D_1, \tag{63}$$

$$H_x = H\otimes I_{N_y}, \quad H_y = I_{N_x}\otimes H, \quad \tilde{H} = H\otimes H = H_xH_y, \tag{64}$$

$$e_W = e_1\otimes I_{N_y}, \quad e_E = e_{N_x}\otimes I_{N_y}, \quad e_S = I_{N_x}\otimes e_1, \quad e_N = I_{N_x}\otimes e_{N_y}, \tag{65}$$

where I_m is an $m\times m$ identity matrix. The operators D_x and D_y are first derivative operators acting in the x and y directions, respectively; H_x and H_y are quadrature operators integrating in respective directions; and e_W, e_E, e_S, and e_N extract the values at the west, east, south, and north boundaries, respectively.

The construction of a 2D narrow-stencil second derivative operator for variable coefficients is more involved. If the variable coefficient term within $D_2^{(a)}$ is spatially variable in both x and y, i.e., $a = a(x, y)$, it is not possible to use the Kronecker product as in Eqs. 63–65. However, using these operators, narrow-stencil second derivative operators can be constructed in the same fashion as in Definitions 5 and 6. A 2D, fully compatible, narrow-stencil, second derivative SBP operator acting in the x direction is

$$D_{2x}^{(a)} = H_x^{-1}(-D_{1x}^T A H_x D_{1x} - R_x^{(a)} + A B_x D_{1x}), \tag{66}$$

where A is an $N_x N_y \times N_x N_y$ matrix with the variable coefficients $a(x, y)$ injected on the diagonal as $A = \text{diag}(a_{1,1}, \dots a_{N_y,1}, a_{1,2}, \dots a_{N_y,2}, \dots, a_{N_y,N_x})$, and $B_x = B \otimes I_{N_y}$. The remainder term $R_x^{(a)}$ is the extension of the remainder term $R^{(a)}$ in the 1D problem (Section 4); for details, see [23]. The second derivative operator in the y direction, $D_{2y}^{(a)}$, is constructed in a similar manner.

One can also use the Kronecker product to extend operators to systems of equations. For a system of k equations, extending an operator P to act on each equation is done by $\mathbf{P} = I_k \otimes P$. In the coming analysis the boldface notation will be used to specifically indicate that an operator is extended to a system of two equations, e.g., $\mathbf{D}_{1x} = I_2 \otimes D_{1x}$.

As a final remark we note two useful properties of the Kronecker product: $(A \otimes B)(C \otimes D) = (AC) \otimes (BD)$ and $(A \otimes B)^T = A^T \otimes B^T$, assuming that the matrix-matrix multiplications AC and BD are defined. This allows for operators acting in different coordinate directions to commute, i.e., $[P_x, Q_y] = 0$ where P_x and Q_y are some operators acting along the x- and y-direction respectively. Although not always stated explicitly, the commutation property will be frequently used in the following stability analysis.

8 Semi-discrete stability in 2D

In this section, the semi-discretizations of the linear poroelastic equations in the pressure and fluid content formulations are presented. Using the SBP-SAT method, semi-discrete stability is shown by deriving a semi-discrete counterpart of the continuous energy estimate in Eq. 50.

8.1 Spatial discretization for the pressure formulation

Discretizing Ω as in Eq. 61, let the length $2N_xN_y$ vector $\mathbf{u} = [u \quad v]^T$ and the length N_xN_y vector p be approximations of their continuous counterparts. The distinction between u, v and p as functions and vectors should be clear from the context. The discretized material coefficient matrices (α, M^{-1}, κ, G, and λ) are diagonal and contain properties evaluated at each grid point. We then construct the $\mathbf{A}, \mathbf{B}$, and $\mathbf{C}$ matrices from G and λ as in Eq. 40. Using the SBP operators in Section 7, the initial-boundary value problem for the linear poroelastic equations

stated in Eqs. 38–41 is discretized using the SBP-SAT method as

$$\begin{aligned} 0 = \mathbf{D}_{2x}^{(A)}\mathbf{u} + \mathbf{D}_{1x}\mathbf{C}\mathbf{D}_{1y}\mathbf{u} + \mathbf{D}_{1y}\mathbf{C}^T\mathbf{D}_{1x}\mathbf{u} + \mathbf{D}_{2y}^{(B)}\mathbf{u} \\ -\hat{x}\otimes(D_{1x}\alpha p) - \hat{y}\otimes(D_{1y}\alpha p) + SAT_1, \end{aligned} \tag{67}$$

$$M^{-1}p_t = D_{2x}^{(\kappa)}p + D_{2y}^{(\kappa)} - (\hat{x}^T\otimes\alpha D_{1x} + \hat{y}^T\otimes\alpha D_{1y})\mathbf{u}_t + SAT_2, \tag{68}$$

with initial conditions $\mathbf{u} = \mathbf{h}_1$, $p = h_2$, $t = 0$, where $\mathbf{h}_1$ and h_2 are the initial condition vectors structured in the same way as $\mathbf{u}$ and p. The SAT terms are

$$\begin{aligned} SAT_1 = \mathbf{H}_x^{-1}\mathbf{e}_W(-(\boldsymbol{\gamma}_W\otimes e_W^T)\mathbf{u} + \mathbf{e}_W^T\mathbf{T}_x + \mathbf{g}_W) \\ +\mathbf{H}_x^{-1}\mathbf{e}_E(-(\boldsymbol{\gamma}_E\otimes e_E^T)\mathbf{u} - \mathbf{e}_E^T\mathbf{T}_x + \mathbf{g}_E) \\ +\mathbf{H}_y^{-1}\mathbf{e}_S(-(\boldsymbol{\gamma}_S\otimes e_S^T)\mathbf{u} + \mathbf{e}_S^T\mathbf{T}_y + \mathbf{g}_S) \\ +\mathbf{H}_y^{-1}\mathbf{e}_N(-(\boldsymbol{\gamma}_N\otimes e_N^T)\mathbf{u} - \mathbf{e}_N^T\mathbf{T}_y + \mathbf{g}_N), \end{aligned} \tag{69}$$

and

$$\begin{aligned} SAT_2 = H_x^{-1}e_W(-\delta_W e_W^T p - q_x p + f_W) + H_x^{-1}e_E(-\delta_E e_e^T p + q_x p + f_E) \\ +H_y^{-1}e_S(-\delta_S e_S^T p - q_y p + f_S) + H_y^{-1}e_N(-\delta_N e_N^T p + q_y p + f_N). \end{aligned} \tag{70}$$

Here $\boldsymbol{\gamma}$ and δ are the SAT penalty parameters. The tractions and discharge velocities are

$$\mathbf{T}_x = (\mathbf{A}\mathbf{D}_{1x} + \mathbf{C}\mathbf{D}_{1y})\mathbf{u} - \hat{x}\otimes(\alpha p), \quad q_x = -\kappa D_{1x}p, \tag{71}$$

$$\mathbf{T}_y = (\mathbf{C}^T\mathbf{D}_{1x} + \mathbf{B}\mathbf{D}_{1y})\mathbf{u} - \hat{y}\otimes(\alpha p), \quad q_y = -\kappa D_{1y}p. \tag{72}$$

The boundary data $\mathbf{g}$ and f are specified according to Eq. 44.

8.2 Semi-discrete stability

In this section, semi-discrete stability of the 2D pressure formulation is shown by deriving a semi-discrete energy estimate that mimicks the continuous energy estimate in Eq. 50. Multiplying Eqs. 67 and 68 by $\mathbf{u}^T\tilde{\mathbf{H}}$ and $p^T\tilde{H}$, respectively, and add their transposes, yields

$$\begin{aligned} \frac{dE_M}{dt} = -u_t^T H_y Q_x \alpha p - p^T \alpha Q_x^T H_y u_t - v_t^T H_x Q_y \alpha p - p^T \alpha Q_y^T H_x v_t \\ -u_t^T e_W H_y e_W^T \alpha p + v_t^T e_E H_y e_E^T \alpha p - u_t^T e_S H_x e_S^T \alpha p + v_t^T e_N H_x e_N^T \alpha p, \end{aligned} \tag{73}$$

$$\begin{aligned} \frac{dE_F}{dt} = -2\|D_x p\|^2_{\tilde{H}\kappa} - 2\|D_y p\|^2_{\tilde{H}\kappa} - 2\|p\|^2_{H_y R_x^{(\kappa)}} - 2\|p\|^2_{H_x R_y^{(\kappa)}} \\ -p^T H_y \alpha Q_x u_t - u_t^T Q_x^T \alpha H_y p - p^T H_x \alpha Q_y v_t - v_t^T Q_y^T \alpha H_x p \\ -2\delta_W \|p_W\|^2_{H_y} - 2\delta_E \|p_E\|^2_{H_y} - 2\delta_S \|p_S\|^2_{H_x} - 2\delta_N \|p_N\|^2_{H_x}, \\ +p^T e_W H_y \alpha e_W^T u_t - p^T e_E H_y \alpha e_E^T u_t + p^T e_S H_x \alpha e_S^T v_t - p^T e_N H_x \alpha e_N^T v_t, \end{aligned} \tag{74}$$

where

$$\begin{aligned} E_M = \|\hat{\mathbf{u}}\|^2_{\hat{\mathbf{H}}\mathbf{P}} + \|\mathbf{u}\|^2_{\mathbf{H_y R}_x^{(A)}} + \|\mathbf{u}\|^2_{\mathbf{H_x R}_y^{(B)}} \\ +\|\mathbf{u}_W\|^2_{\boldsymbol{\gamma}_W\otimes H_y} + \|\mathbf{u}_E\|^2_{\boldsymbol{\gamma}_E\otimes H_y} + \|\mathbf{u}_S\|^2_{\boldsymbol{\gamma}_S\otimes H_x} + \|\mathbf{u}_N\|^2_{\boldsymbol{\gamma}_N\otimes H_x} \end{aligned} \tag{75}$$

is the energy contribution from the mechanical equilibrium equation and

$$E_F = \|p\|^2_{\tilde{H}M^{-1}} \tag{76}$$

is the energy contribution from the fluid diffusion equation. The vector $\hat{\mathbf{u}}$ and matrix $\hat{\mathbf{H}}$ are defined as

$$\hat{\mathbf{u}} = \begin{bmatrix} \mathbf{D}_x\mathbf{u} \\ \mathbf{D}_y\mathbf{u} \end{bmatrix}, \quad \hat{\mathbf{H}} = \begin{bmatrix} \tilde{\mathbf{H}} & 0 \\ 0 & \tilde{\mathbf{H}} \end{bmatrix} \tag{77}$$

and $\mathbf{P}$ is the discrete version of Eq. 47. In order to obtain $\|\hat{\mathbf{u}}\|^2_{\hat{\mathbf{H}}\mathbf{P}}$ in Eq. 73 it is required that $\mathbf{C}$ and $\tilde{\mathbf{H}}$ commute, which can be shown using the block-diagonal structure of $\mathbf{C}$. To obtain a semi-discrete energy estimate we make use of the relations $Q_x + Q_x^T = 0$ and $Q_y + Q_y^T = 0$ and that operators acting in different coordinate directions commute. Adding Eqs. 73 and 74, and making use of the mentioned relations, results in the semi-discrete energy estimate for system:

$$\begin{aligned} \frac{dE}{dt} = &-2\|D_x p\|^2_{\tilde{H}\kappa} - 2\|D_y p\|^2_{\tilde{H}\kappa} - 2\|p\|^2_{H_y R_x^{(\kappa)}} - 2\|p\|^2_{H_x R_y^{(\kappa)}} \\ &-2\delta_W\|p_W\|^2_{H_y} - 2\delta_E\|p_E\|^2_{H_y} - 2\delta_S\|p_S\|^2_{H_x} - 2\delta_N\|p_N\|^2_{H_x}, \end{aligned} \tag{78}$$

where $E = E_M + E_F$ is the semi-discrete energy. It is clear that Eq. 78 is the semi-discrete counterpart of the continuous energy estimate (Eq. 50). Note that if $\boldsymbol{\gamma} \geq 0$ and $\delta \geq 0$, then $E \geq 0$ and $dE/dt \leq 0$ and hence semi-discrete stability for Eqs. 67–68 using the SBP-SAT method is proven. The penalty parameters are written, as in the 1D case, as dimensionless constants scaled by grid spacing and some appropriate material property:

$$\boldsymbol{\gamma}_W = \boldsymbol{\gamma}_E = \frac{\gamma_x^*}{\Delta x}\mathbf{A}, \quad \boldsymbol{\gamma}_S = \boldsymbol{\gamma}_N = \frac{\gamma_y^*}{\Delta y}\mathbf{B}, \tag{79}$$

$$\delta_W = \delta_E = \frac{\delta_x^*}{\Delta x}\kappa, \quad \delta_S = \delta_N = \frac{\gamma_y^*}{\Delta y}\kappa, \tag{80}$$

where γ_x^*, $\delta_x^* = N_x^{p-1}$ and γ_y^*, $\delta_y^* = N_y^{p-1}$ for pth order accuracy at a Dirichlet boundary. When imposing Neumann conditions $\boldsymbol{\gamma}, \delta$ are set to zero.

8.3 Spatial discretization for the fluid content formulation

This section presents the fluid content formulation of the linear poroelastic equations in 2D, discretized using the SBP-SAT method. We prove equivalence of the fluid content and pressure formulations, from which stability follows from the analysis of Section 8.2. The discrete version of Eq. 55 is $p_u = -M\alpha(\hat{x}^T \otimes D_{1x} + \hat{y}^T \otimes \alpha D_{1y})\mathbf{u}$, such that

$$p = p' + p_u = p' - M\alpha(\hat{x}^T \otimes D_{1x} + \hat{y}^T \otimes \alpha D_{1y})\mathbf{u}. \tag{81}$$

The initial-boundary value problem in the fluid content formulation (Eqs. 56–58), discretized using the SBP-SAT method, is

$$\begin{aligned} 0 = &\mathbf{D}_{2x}^{(A_u)}\mathbf{u} + \mathbf{D}_{1x}\mathbf{C}_u\mathbf{D}_{1y}\mathbf{u} + \mathbf{D}_{1y}\mathbf{C}_u^T\mathbf{D}_{1x}\mathbf{u} + \mathbf{D}_{2y}^{(B_u)}\mathbf{u} + \bar{R}\mathbf{u} \\ &-\hat{x} \otimes (D_{1x}\alpha p') - \hat{y} \otimes (D_{1y}\alpha p') + SAT_1, \end{aligned} \tag{82}$$

$$M^{-1}p'_t = \left(D_{2x}^{(\kappa)} + D_{2y}^{(\kappa)}\right)\left(p' - M\alpha\left(\hat{x}^T \otimes D_{1x} + \hat{y}^T \otimes \alpha D_{1y}\right)\mathbf{u}\right) + SAT_2, \quad (83)$$

where

$$\bar{R} = \mathrm{diag}(1,0) \otimes \left(H_x^{-1} R_x^{(M\alpha^2)}\right) + \mathrm{diag}(0,1) \otimes \left(H_y^{-1} R_y^{(M\alpha^2)}\right) \quad (84)$$

and

$$-\left(D_{2x}^{(\kappa)} + D_{2y}^{(\kappa)}\right) M\alpha\left(\hat{x}^T \otimes D_{1x} + \hat{y}^T \otimes \alpha D_{1y}\right)\mathbf{u} \quad (85)$$

are the 2D versions of the interior penalty terms in Section 5. The initial conditions for the fluid content formulation in 2D are $\mathbf{u} = \mathbf{h}_1$, $p' = h_2 + M\alpha(\hat{x}^T \otimes D_{1x} + \hat{y}^T \otimes \alpha D_{1y})\mathbf{h}_1$, $t = 0$. The undrained material coefficient matrices $\mathbf{A}_u$, $\mathbf{B}_u$, and $\mathbf{C}_u$ are obtained from the drained material coefficient matrices $\mathbf{A}$, $\mathbf{B}$, and $\mathbf{C}$, by replacing λ with $\lambda_u = \lambda + M\alpha^2$. The SAT terms are

$$\begin{aligned} SAT_1 &= \mathbf{H}_x^{-1}\mathbf{e}_W(-\boldsymbol{\gamma}_W \otimes e_W^T\mathbf{u} + \mathbf{e}_W^T\mathbf{T}_x + \mathbf{g}_W) + \mathbf{H}_x^{-1}\mathbf{e}_E(-\boldsymbol{\gamma}_E \otimes e_E^T\mathbf{u} - \mathbf{e}_E^T\mathbf{T}_x + \mathbf{g}_E) \\ &\quad + \mathbf{H}_y^{-1}\mathbf{e}_S(-\boldsymbol{\gamma}_S \otimes e_S^T\mathbf{u} - \mathbf{e}_S^T\mathbf{T}_y + \mathbf{g}_S) + \mathbf{H}_y^{-1}\mathbf{e}_N(-\boldsymbol{\gamma}_N \otimes e_N^T\mathbf{u} - \mathbf{e}_N^T\mathbf{T}_y + \mathbf{g}_N), \quad (86) \\ SAT_2 &= H_x^{-1}e_W(-\delta_W e_W^T p - q_x p + f_W) + H_x^{-1}e_E(-\delta_E e_e^T p + q_x p + f_E) \\ &\quad + H_y^{-1}e_S(-\delta_S e_S^T p - q_y p + f_S) + H_y^{-1}e_N(-\delta_N e_N^T p + q_y p + f_N). \quad (87) \end{aligned}$$

Note that the SAT terms are identical to those presented in Eqs. 69 and 70. The SAT terms can be expressed in terms of p' and u, using Eq. 81 with the traction vectors and discharge velocities written as

$$\mathbf{T}_x = (\mathbf{A}_u\mathbf{D}_{1x} + \mathbf{C}_u\mathbf{D}_{1y})\mathbf{u} - \hat{x} \otimes (\alpha p'), \quad (88)$$

$$\mathbf{T}_y = (\mathbf{B}_u\mathbf{D}_{1y} + \mathbf{C}_u^T\mathbf{D}_{1x})\mathbf{u} - \hat{y} \otimes (\alpha p'), \quad (89)$$

$$q_x = -D_{1x}\kappa(p' - M\alpha(\hat{x}^T \otimes D_{1x} + \hat{y}^T \otimes \alpha D_{1y})\mathbf{u}), \quad (90)$$

$$q_y = -D_{1y}\kappa(p' - M\alpha(\hat{x}^T \otimes D_{1x} + \hat{y}^T \otimes \alpha D_{1y})\mathbf{u}). \quad (91)$$

Analogously to the 1D case, it can be shown [45] that the semi-discrete fluid content and pressure formulations are exactly equivalent. Stability follows immediately from the results in Section 8.2.

9 Time integration with linear boundary conditions

Spatial discretization of the linear poroelastic equations with the SBP-SAT method yields a system of differential algebraic equations (DAEs) that can be solved using an appropriate time integrator. For linear boundary conditions of the form examined thus far (i.e., Dirichlet or Neumann conditions with known data), the DAEs are also linear. This section briefly explains the time-stepping methods used for this class of problems. In contrast, frictional dynamics, which we introduce in Section 12, introduces nonlinearities and additional differential equations that must be solved simultaneously with the poroelastic equations. More sophisticated time-stepping procedures are necessary in that case, but for now we focus on the simpler linear problem.

The pressure formulation requires an implicit time integrator. In this work we use the fourth order accurate backward differentiation formula multistep method [15], hereafter referred to as BDF4. In contrast, the fluid content formulation can

be advanced in time using an explicit time-stepping method for the fluid diffusion equation in combination with a linear system solve for the mechanical equilibrium equation. We use the standard fourth order explicit Runge-Kutta method [14], hereafter referred to as RK4. For the linear problem, the fluid content formulation is approximately 1.5 times faster than the pressure formulation when using the same time step, at least when using direct solvers. This is exactly what is expected based on the computational complexity being dominated by linear system solves.

The spectral radius of the evolution matrix for the discrete equations can be examined to quantify stiffness and to determine the maximum stable time step for explicit methods. Imposing boundary conditions using the Robin method affects the stiffness of the system. We find that Dirichlet conditions lead to stiffer systems compared to Neumann conditions, due to the fact that the penalty terms δ and γ introduced in Section 5 scale some of the eigenvalues in the system. There is a trade-off: more accurate Dirichlet conditions result in a stiffer system. Through a study of the eigenvalues and stiffness for model problems (not reported here in the interest to space), we found that for the problems, parameter values, and penalty parameters considered in this work it suffices to select a time step based solely on consideration of the pore pressure diffusion equation. That is, we choose a time step to be smaller than approximately $\Delta x^2/c$, where $c = \kappa M$ is the hydraulic diffusivity.

10 Verification using the method of manufactured solutions

We now verify convergence and accuracy of the numerical scheme using the method of manufactured solutions (MMS) [37]. In MMS, the solution fields are chosen arbitrarily and will not necessarily satisfy the governing equations by themselves. Therefore, the differences that arise from inserting the manufactured solution fields into the governing equations are added to the equations as boundary data and source terms. With these additions the manufactured solutions satisfy the modified linear poroelastic equations.

The MMS problem is representative in scale of a laboratory experiment. The domain is the unit square $\Omega = \{(x, y) : 0 \leq x \leq 1 \text{ m}, 0 \leq y \leq 1 \text{ m}\}$ and the manufactured solution is

$$u = \sin(\pi x)\sin(\pi y)\cos(1000\pi t)\ \mu\text{m}, \tag{92}$$

$$v = \sin(\pi x)\sin(\pi y)\cos(1000\pi t)\ \mu\text{m}, \tag{93}$$

$$p = \sin(\pi x)\sin(\pi y)\cos(1000\pi t)\ \text{kPa}. \tag{94}$$

Boundary conditions for this problem are imposed using either Neumann and Dirichlet conditions on the different boundaries (Table 1), where the boundary data are obtained from the solution (Eqs. 92–94). The initial conditions are obtained by evaluating the solution at $t = 0$.

Table 1 Boundary conditions imposed for the MMS verification tests. Here D signifies Dirichlet conditions, N signifies Neumann conditions, M_1 and M_2 signify the first and second equations in the mechanical equilibrium equations and F signifies the fluid diffusion equation.

Type	M_1	M_2	F
West	N	D	N
East	D	N	D
South	N	D	D
North	D	N	N

The poroelastic parameters are spatially variable:

$$\lambda = 1 + 0.5\sin(\pi x)\cos(\pi y) \text{ GPa}, \tag{95}$$
$$G = 1 + 0.5\cos(\pi x)\sin(\pi y) \text{ GPa}, \tag{96}$$
$$M = 1 + 0.8\sin(\pi x)\sin(\pi y) \text{ GPa}, \tag{97}$$
$$\alpha = 0.7 + 0.2\sin(\pi x)\cos(\pi y), \tag{98}$$
$$\kappa = 0.001 + \cos(0.5\pi x)\cos(0.5\pi y) \text{ m}^2/(\text{GPa s}), \tag{99}$$

Since the mobility κ often varies over several orders of magnitude in real applications, its variability is chosen to be considerably larger than for other parameters.

A convergence study is conducted by solving the modified linear poroelastic equations in the pressure formulation (Eqs. 38 and 39) with the following spatial resolutions (in both the x- and y-direction): $N = N_x = N_y = 10, 20, \ldots, 80$. The system is integrated in time from $t = 0$ to 10^{-7} s using BDF4 with N time steps. The global error at the final time is measured for each grid spacing in the H-norm,

$$\|e_u^m\|_H = (e_u^m)^T \tilde{H} e_u^m, \tag{100}$$

where m is the total number of unknowns, $\tilde{H} = H \otimes H$ is the quadrature matrix defined in Section 7, and e_u^m is an $N_x N_y$ column vector with the local errors as entries. The convergence rate q when increasing the number of unknowns from m_1 to m_2 is defined as

$$q_u = \log_{10}\left(\frac{\|e_u^{m_1}\|_H}{\|e_u^{m_2}\|_H}\right) \Big/ \log_{10}\left(\frac{m_2}{m_1}\right)^{\frac{1}{d}}, \tag{101}$$

where d is the dimension ($d = 2$ in this case) [24].

The convergence test is carried out for both the second order operators with second order Dirichlet conditions (Table 2) and fourth order operators with third order Dirichlet conditions (Table 3); converge rates match theoretical expectations (second order and third order, respectively).

Next we perform a convergence test for the fluid content formulation using the same manufactured solution, boundary and initial conditions, and forcing, but with explicit RK4 time integration. While the solution is obtained in terms of u, v, and p', the latter is converted to p using Eq. 55 since this is typically the quantity of interest. Errors and convergence rates, presented in Tables 2–5, demonstrate that the two formulations are very similar in terms of accuracy.

Table 2 Convergence rates for the horizontal displacement u, the vertical displacement v, and the pore pressure p in the modified linear poroelastic problem using the pressure formulation and the implicit BDF4 time integrator. The table shows the logarithmic error in the H-norm and the convergence rate q for the $N \times N$ spatial grids, discretized using second order accurate SBP operators with second order accurate Dirichlet boundary conditions.

N	$\log_{10}(\|e_u^m\|_H)$	q_u	$\log_{10}(\|e_v^m\|_H)$	q_v	$\log_{10}(\|e_p^m\|_H)$	q_p
10	-1.5338	×	-1.5735	×	-1.4454	×
20	-2.1807	2.1489	-2.2194	2.1457	-2.0929	2.1508
30	-2.5482	2.0865	-2.5864	2.0841	-2.4600	2.0850
40	-2.8057	2.0613	-2.8437	2.0592	-2.7173	2.0588
50	-3.0041	2.0475	-3.0419	2.0458	-2.9154	2.0450
60	-3.1656	2.0387	-3.2032	2.0373	-3.0767	2.0366
70	-3.3016	2.0327	-3.3392	2.0315	-3.2127	2.0309
80	-3.4193	2.0283	-3.4568	2.0273	-3.3302	2.0268

Table 3 Convergence rates for the horizontal displacement u, the vertical displacement v and the pore pressure p in the modified linear poroelastic problem using the pressure formulation and the implicit BDF4 time integrator. The table shows the logarithmic error in the H-norm and the convergence rate q for the $N \times N$ spatial grids, discretized using fourth order accurate SBP operators with third order accurate Dirichlet boundary conditions.

N	$\log_{10}(\|e_u^m\|_H)$	q_u	$\log_{10}(\|e_v^m\|_H)$	q_v	$\log_{10}(\|e_p^m\|_H)$	q_p
10	-2.6840	×	-2.6346	×	-2.2843	×
20	-3.7764	3.6290	-3.6439	3.3528	-3.4736	3.9508
30	-4.3262	3.1222	-4.1774	3.0296	-4.1289	3.7215
40	-4.7079	3.0549	-4.5533	3.0089	-4.5908	3.6967
50	-5.0023	3.0379	-4.8448	3.0071	-4.9319	3.5206
60	-5.2421	3.0286	-5.0829	3.0077	-5.1933	3.3009
70	-5.4445	3.0237	-5.2843	3.0078	-5.4096	3.2310
80	-5.6198	3.0229	-5.4586	3.0068	-5.5949	3.1948

Table 4 Convergence rates for the horizontal displacement u, the vertical displacement v and the pore pressure p in the modified linear poroelastic problem using the fluid content formulation and the explicit RK4 time integrator. The table shows the logarithmic error in the H-norm and the convergence rate q for the $N \times N$ spatial grids, discretized second order accurate SBP operators with second order accurate Dirichlet boundary conditions.

N	$\log_{10}(\|e_u^m\|_H)$	q_u	$\log_{10}(\|e_v^m\|_H)$	q_v	$\log_{10}(\|e_p^m\|_H)$	q_p
10	-1.5338	×	-1.5735	×	-1.4454	×
20	-2.1807	2.1489	-2.2194	2.1457	-2.0929	2.1508
30	-2.5482	2.0865	-2.5864	2.0841	-2.4600	2.0850
40	-2.8057	2.0613	-2.8437	2.0592	-2.7172	2.0588
50	-3.0041	2.0475	-3.0419	2.0458	-2.9154	2.0450
60	-3.1656	2.0387	-3.2032	2.0373	-3.0767	2.0365
70	-3.3016	2.0327	-3.3392	2.0315	-3.2126	2.0308
80	-3.4193	2.0283	-3.4568	2.0273	-3.3302	2.0267

11 Mandel's problem

This section presents Mandel's problem, a canonical poroelastic problem for which analytical solutions [5,2] are available. We perform a convergence study using the pressure formulation (Section 8.1). We also performed a similar study using the explicit fluid content formulation. We obtained very similar results, so only present the pressure formulation results here.

Table 5 Convergence rates for the horizontal displacement u, the vertical displacement v and the pore pressure p in the modified linear poroelastic problem using the fluid content formulation and the explicit RK4 time integrator. The table shows the logarithmic error in the H-norm and the convergence rate q for the $N \times N$ spatial grids, discretized using fourth order accurate SBP operators with third order accurate Dirichlet boundary conditions.

N	$\log_{10}(\|e_u^m\|_H)$	q_u	$\log_{10}(\|e_v^m\|_H)$	q_v	$\log_{10}(\|e_p^m\|_H)$	q_p
10	-2.6840	×	-2.6346	×	-2.2842	×
20	-3.7764	3.6289	-3.6439	3.3528	-3.4727	3.9479
30	-4.3261	3.1220	-4.1774	3.0297	-4.1261	3.7109
40	-4.7078	3.0552	-4.5534	3.0088	-4.5900	3.7131
50	-5.0023	3.0381	-4.8448	3.0070	-4.9320	3.5292
60	-5.2421	3.0285	-5.0829	3.0077	-5.1933	3.3001
70	-5.4445	3.0238	-5.2843	3.0077	-5.4096	3.2307
80	-5.6198	3.0230	-5.4586	3.0068	-5.5949	3.1946

In Mandel's problem a rectangular and infinitely long plate of poroelastic material is placed between two impermeable and rigid plates, located at the south and north boundaries. The plates are free to slide horizontally with zero shear traction. The west and east boundaries are traction free and drained (i.e., $p = 0$). At time $t = 0$ a compressive force $\mathbf{F}$ is applied and held constant at the two rigid plates, such that $\int_{-a}^{a} \sigma_{yy}(x, b, t)dx = -F$.

The problem is symmetric both in the x- and the y-directions, and therefore it is sufficient to model one quarter of the domain:

$$\Omega = \{(x, y) : 0 \leq x \leq a, 0 \leq y \leq b\}. \tag{102}$$

On the west and south boundaries of the domain defined in Eq. 102, the boundary conditions are imposed as symmetry conditions. For clarity, the boundary conditions are

$$q_x = 0, \quad u = 0, \quad \sigma_{xy} = 0, \quad (x, y) \in \Omega_W, \tag{103}$$

$$p = 0, \quad \sigma_{xx} = 0, \quad \sigma_{xy} = 0, \quad (x, y) \in \Omega_E, \tag{104}$$

$$q_y = 0, \quad \sigma_{xy} = 0, \quad v = 0, \quad (x, y) \in \Omega_S, \tag{105}$$

$$q_y = 0, \quad \sigma_{xy} = 0, \quad \int_{-a}^{a} \sigma_{yy}(x, b, t)dx = -F, \quad (x, y) \in \Omega_N. \tag{106}$$

One approach for imposing the boundary condition involving the compressive force F is to specify σ_{yy} as a Neumann condition with the integral approximated using the quadrature property of the SBP operators. Another approach is to use the analytical solution for either σ_{yy} or v at the boundary. Here, we impose the analytical v as a Dirichlet boundary condition. The initial conditions are set to the analytical solutions at the start of the simulations. Since the pore pressure p in Mandel's problem has a sharp spatial gradient close to the east boundary for early times, the simulations are not started at $t = 0$, but at some slightly later time. The solution is calculated for dimensionless parameters $a/b = 1$, $B = 0.8$, $\nu = 0.2$, and $\nu_u = 0.4$. The remaining parameters and choice of F are irrelevant as the solution results are presented in nondimensional form.

Mandel's problem is simulated using the pressure formulation on a 20×20 grid, using fourth order SBP operators and third order Dirichlet conditions, from dimensionless time $t^* = 10^{-4}$ to $t^* = 10^{-1}$ using 1000 equidistant time steps with the BDF4 scheme, where $t^* = ct/a^2$. The numerical and analytical solutions

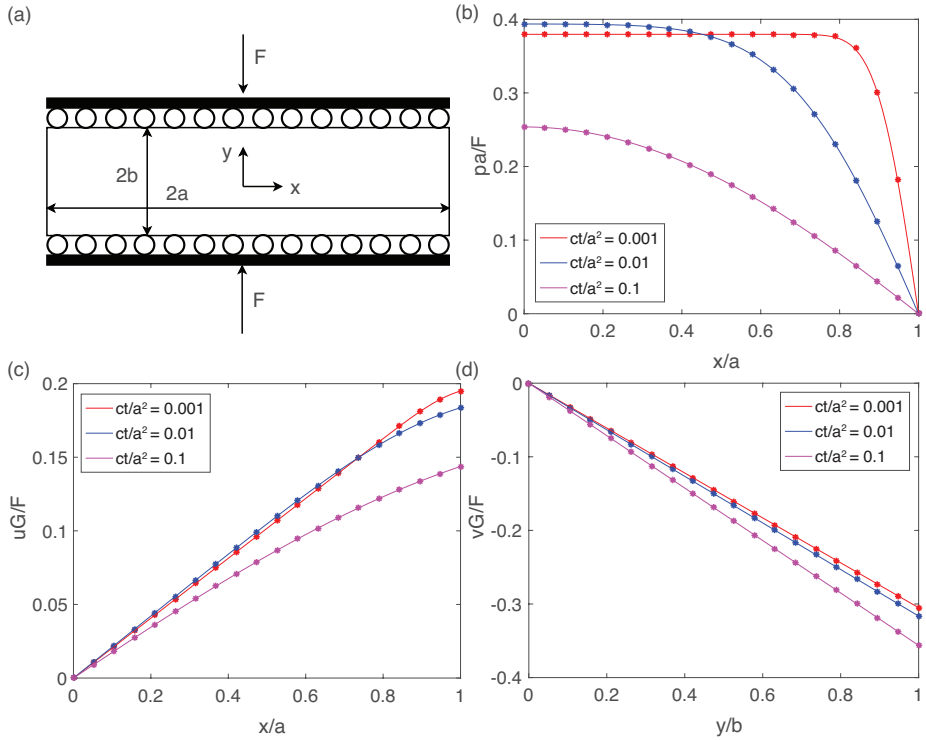

Fig. 1 (a) Mandel's problem: A compressive force F is applied by squeezing a porous solid with a rigid, frictionless, impermeable plate, with drained ($p = 0$) and traction-free ($\sigma_{xx} = \sigma_{xy} = 0$) boundary conditions on the left and right sides. (b)-(d) Comparison of analytical (solid lines) and numerical (asterisks) solutions with the pressure formulation, discretized using the BDF4 time integrator and the fourth order SBP operators with third order Dirichlet conditions.

are compared in Figure 1; the only visible discrepancies occur within the pressure boundary layer at early times. Note also that the nonmonotonic pressure response in Figure 1c is the famous poroelastic phenomenon known as the Mandel–Cryer effect.

Convergence for Mandel's problem is demonstrated with a set of pressure formulation simulations using $N = 10, 20, \ldots, 80$ spatial points in both the x- and the y-directions, from $t^* = 10^{-3}$ to $t^* = 1.0001 \times 10^{-3}$ using N number of equidistant time steps with the BDF4 time integrator. The convergence rates for the second order SBP operators with second order accurate Dirichlet conditions and the fourth order SBP operators with third order accurate Dirichlet conditions are reported in Tables 6 and 7, respectively. Somewhat irregular convergence behavior for p on the coarser grids is likely due to the challenge of resolving the boundary layer. However, with sufficient grid refinement, the expected global second and third order convergence rates are realized for all fields.

Table 6 Convergence rates for the normalized horizontal displacement u^*, the normalized vertical displacement v^*, and the normalized pore pressure p^* in Mandel's problem using the pressure formulation and the implicit BDF4 time integrator. The table shows the logarithmic error in the H-norm and the convergence rate q for the $N \times N$ spatial grids, discretized using second order accurate SBP operators with second order accurate Dirichlet boundary conditions.

N	$\log_{10}(\|e_u^m\|_H)$	q_u	$\log_{10}(\|e_v^m\|_H)$	q_v	$\log_{10}(\|e_p^m\|_H)$	q_p
10	-2.4881	×	-2.6231	×	-1.9718	×
20	-3.1050	2.0491	-3.2437	2.0616	-2.6175	2.1449
30	-3.4634	2.0354	-3.6027	2.0384	-2.9739	2.0239
40	-3.7166	2.0267	-3.8560	2.0278	-3.2265	2.0219
50	-3.9125	2.0213	-4.0519	2.0217	-3.4223	2.0199
60	-4.0722	2.0177	-4.2117	2.0178	-3.5818	2.0154
70	-4.2072	2.0151	-4.3466	2.0151	-3.7163	2.0081
80	-4.3239	2.0132	-4.4634	2.0131	-3.8321	1.9975

Table 7 Convergence rates for the normalized horizontal displacement u^*, the normalized vertical displacement v^*, and the normalized pore pressure p^* in Mandel's problem using the pressure formulation and the implicit BDF4 time integrator. The table shows the logarithmic error in the H-norm and the convergence rate q for the $N \times N$ spatial grids, discretized using fourth order accurate SBP operators with third order accurate Dirichlet boundary conditions.

N	$\log_{10}(\|e_u^m\|_H)$	q_u	$\log_{10}(\|e_v^m\|_H)$	q_v	$\log_{10}(\|e_p^m\|_H)$	q_p
10	-3.5330	×	-3.6170	×	-2.1922	×
20	-4.3825	2.8218	-4.5434	3.0772	-2.8107	2.0545
30	-4.9440	3.1889	-5.0792	3.0430	-3.6341	4.6761
40	-5.3157	2.9747	-5.4577	3.0298	-3.8360	1.6161
50	-5.6076	3.0120	-5.7507	3.0229	-4.0502	2.2100
60	-5.8487	3.0448	-5.9897	3.0186	-4.2688	2.7608
70	-6.0531	3.0532	-6.1916	3.0157	-4.4701	3.0070
80	-6.2300	3.0509	-6.3664	3.0136	-4.6528	3.1497

12 Fluid-induced earthquakes

A primary objective of the present study is to develop a numerical method for modeling induced seismicity, specifically problems of earthquake nucleation due to fluid injection or extraction, in the context of a fully coupled poroelastic model. This section introduces the frictional framework used for modeling slip on faults, extends the numerical method to handle frictional fault dynamics, and then illustrates modeling capabilities with an example problem. In this problem fault slip is triggered by fluid injection and flow through a permeable damage zone surrounding the fault. We demonstrate how frictional properties control whether fault slip occurs seismically or aseismically.

A fault is commonly idealized as an interface between two poroelastic solids, with interface conditions capturing fault dynamics (i.e., a friction law relating shear and normal tractions and pore pressure, force balance for tractions on opposing sides of the fault, and a requirement that the two sides of the fault remain in contact while effective normal stress remains compressive). In certain cases, the computational model can be limited to a single poroelastic block, using boundary conditions instead of interface conditions. These cases arise for either symmetry in material parameters and loading across the fault or sliding on a rigid substrate. We restrict attention to the latter case in the present study, for ease of implementation, and place the fault at the south boundary ($y = 0$).

The linear poroelastic equations are derived using a quasi-static approximation for the momentum balance (Eq. 3), implying that inertial terms are neglected. However, it is essential to account, at least approximately, for inertial effects during unstable fault slip in earthquakes. A convenient procedure, widely used in simulations of earthquake sequences, is the quasi-dynamic approximation [33]. Rather than adding inertial terms to the mechanical equilibrium equation, the quasi-static equilibrium equations are still solved but a "radiation-damping" term is added to the quasi-static fault shear traction when calculating the shear traction used in the fault friction law. The radiation-damping term accounts for stress changes associated with plane shear waves radiated normal to the fault [33].

12.1 Rate-and-state friction

Slip on faults is commonly modeled by balancing the fault shear stress τ, arising from elastic deformation of the solid, with frictional shear strength $f\sigma'$:

$$\tau = f\sigma', \tag{107}$$

where f is the friction coefficient and σ' is the Terzaghi effective normal stress on the fault, given by

$$\sigma' = \sigma'_0 - \sigma_{yy}\big|_{y=0} - p\big|_{y=0}, \tag{108}$$

where σ'_0 is the background or initial effective normal stress on the fault and σ_{yy} is the change in total normal stress resulting from loading and fault slip as given by Eq. 37. Note that we have defined σ' to be positive in compression, the opposite sign convention from σ_{yy} and other normal stress tensor components. Furthermore the shear stress τ is defined as

$$\tau = \tau_0 + \sigma_{xy}\big|_{y=0} - \eta V, \tag{109}$$

where τ_0 is the background or initial shear stress, σ_{xy} is the change in shear stress resulting from loading and fault slip as given by Eq. 37, and ηV is the radiation-damping term. In the radiation-damping term, η is the impedance of shear waves radiating away from the fault, and V is the slip velocity. When sliding occurs between two identical solids, $\eta = G/2c_s$, where c_s is the shear wave speed, and the slip velocity V is defined as the discontinuity of tangential particle velocity across the fault (at $y = 0$): $V = u_t\big|_{y=0^+} - u_t\big|_{y=0^-}$. For sliding on a rigid substrate, as in the example problems below, $\eta = G/c_s$ and $V = u_t\big|_{y=0}$.

In rate-and-state friction, the friction coefficient f is a function of slip velocity V and a state variable Ψ (e.g., [35]):

$$f(V, \Psi) = a \sinh^{-1}\left(\frac{V}{2V_0} e^{\frac{\Psi}{a}}\right), \tag{110}$$

where $a > 0$ is the dimensionless direct effect parameter and V_0 is an arbitrarily chosen reference velocity. The state variable Ψ is a dimensionless measure of the interface contact strength, as related to the past history of sliding. In this study, the time evolution of Ψ is governed by the slip law,

$$\Psi_t = -\frac{V}{d_c}\left(f - f_0 + (b - a)\ln\left(\frac{V}{V_0}\right)\right), \tag{111}$$

where $d_c > 0$ is the state evolution distance, $b > 0$ is the dimensionless state evolution parameter, and f_0 is the reference friction coefficient for sliding at velocity V_0. The parameter combination $a - b$ determines whether the frictional process is steady state velocity weakening ($a - b < 0$) or steady state velocity strengthening ($a - b > 0$). Discussions of rate-and-state friction, and other possible forms of the state evolution law, can be found in [39,36,22,35].

Inserting Eqs. 109 and 110 into Eq. 107 results in a nonlinear equation for V, which can be solved (using bisection, Newton-Raphson, or a similar method) assuming that the state Ψ is known. Discussion of an efficient bracketed Newton-Raphson method with guaranteed convergence can be found in [20].

Fault sliding is stable for velocity-strengthening friction, but can become unstable at sufficiently long wavelengths for velocity-weakening friction. Linear stability analysis of small perturbations about steady sliding between identical solids reveals a critical length scale,

$$h_f = \frac{\pi G d_c}{\sigma'(b-a)}, \tag{112}$$

that governs stability properties. Many studies [33,21] have demonstrated that this length scale must be well resolved ($\Delta x \ll h_f$, where Δx is the fault grid spacing) for accurate numerical solutions. This length scale also governs whether fault slip stably or unstably in response to gradually applied loading, as we explain with reference to the example simulations below.

12.2 Time integration with rate-and-state friction

The interplay between rate-and-state friction and elasticity gives rise to slip velocities V that vary over many orders of magnitude. Since state evolution occurs over time scales d_c/V, efficient simulations require adaptive time stepping. Generally speaking, we find that in most reasonably discretized application problems the frictional time scales are shorter than the maximum stable time step required for explicit solution of pore pressure diffusion (Section 9). This motivates use of the fluid content formulation, rather than the pressure formulation, together with an explicit, adaptive Runge–Kutta time-stepping method. We use an adaptive 3(2) Runge–Kutta method [14] with error control on fault slip (with a tolerance of 10^{-5} on L_∞ relative error).

To explain the time-stepping procedure, we define the slip δ via the differential equation

$$\delta_t = V \tag{113}$$

and describe the method in terms of a forward Euler update. The generalization to an adaptive Runge–Kutta method is straightforward and discussed elsewhere [16,13].

0. At time $t = t_n$ all fields are known.
1. Integrate p', Ψ, δ to $t + \Delta t$ explicitly in time using the fluid diffusion equation (Eq. 83), the state evolution equation (Eq. 111), and the slip velocity equation (Eq. 113), respectively.
2. Solve the mechanical equilibrium equation (Eq. 82) for $\mathbf{u}$ at $t + \Delta t$, using δ and p' at time $t + \Delta t$, where δ is imposed at the south boundary with a Dirichlet condition.

3. Compute p, σ_{xy}, and σ' at $t + \Delta t$ from $\mathbf{u}$ and p'.
4. Set fault stress equal to frictional strength (Eq. 107) and solve for V at $t + \Delta t$, using σ_{xy}, σ', and Ψ at $t + \Delta t$, and determine τ. Now all fields are known at $t + \Delta t$. Repeat steps 1–4 until the final time is reached.

12.3 Fault slip triggered by injection into a permeable damage zone

We now present a set of simulations illustrating the coupling between poroelastic deformation, fluid diffusion, and fault slip. Fluid influx into a prestressed porous solid through a high permeability "damage zone" surrounding the fault increases pore pressure, weakening the fault and triggering slip. Slight differences in frictional parameters, which make the nucleation length associated with the frictional length scale h_f (Eq. 112) either smaller or larger than the fault length, lead to either unstable or stable fault slip (i.e., earthquakes or slow slip events).

The geometry and boundary conditions are illustrated in Figure 2a. The computational domain is an 8 m × 4 m rectangle with a fault on the south boundary. Slip is only permitted in the central 4 m section of the fault; slip is set identically to zero outside this region. The material parameters are $G = 30$ GPa, $\lambda = 20$ GPa, $\lambda_u = 58.24$ GPa, $\alpha = 0.8145$, $\eta = 4.41$ MPa/(m/s); and the frictional parameters are $a = 0.015$, $b = 0.02$, $V_0 = 10^{-6}$ m/s, $f_0 = 0.6$, and $d_c = 10$, 40, or 80 μm. The medium has initial shear stress $\tau_0 = 30$ MPa, effective normal stress $\sigma_0' = 50$ MPa, and initial state variable $\Psi = 0.606$. This shear stress will cause right-lateral slip (i.e., displacement to right or $u > 0$)

Fluid is injected with a constant pressure gradient, $-p_x = 400$ Pa/m, through the west boundary. The damage zone, of thickness 0.4 m, has $\kappa = 0.025$ m^2/(GPa s) (yielding a hydraulic diffusivity of $c = 0.97$ m^2/s, consistent with recent studies [18], or a permeability of 25 md for water with viscosity 10^{-3} Pa s), while the surrounding region has a κ that is 100 times smaller. The fault surface is impermeable and the modeled poroelastic block slides on a rigid substrate. All problems are run on a 200×200 grid using the second order SBP operators and with second order Dirichlet boundary conditions imposed using the Robin technique. The simulations are run for sufficient time that an earthquake (or aseismic slip) occurs.

Figure 2b shows the evolution of maximum slip velocity on the fault, using a logarithmic scale to emphasize the dramatic increase in slip velocity during earthquakes. Earthquakes occur for $d_c = 10$ and 40 μm, with peak slip velocities reaching approximately 1 m/s, whereas slip velocity remains below 1 mm/s for $d_c = 80$ μm. The adaptive time-stepping procedure provides accuracy even during earthquakes.

Despite the dramatic differences in slip velocity, the total slip is nearly identical in all simulations (Figure 2c). That figure also shows the relatively constant accumulation of slip for the $d_c = 80$ μm case, in contrast to the other two cases involving unstable slip (Figure 2d).

To better understand how fluid injection triggers slip, we show snapshots of pore pressure evolution in the porous solid in Figure 3. In response to injection at a constant pressure gradient on the left side, fluid diffuses into the medium, particularly along the fault damage zone. Pore pressure increases, decreasing effective normal stress (Figure 4a). The initial changes follow the expected scaling for a diffusion process, for which penetration distance scales as $x = \sqrt{ct}$, where c

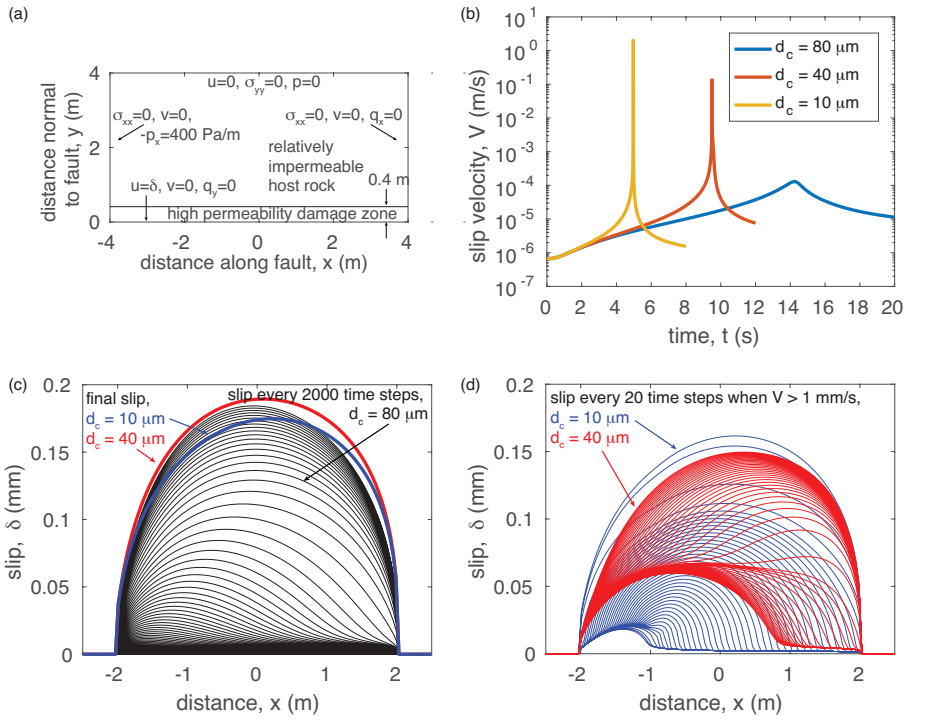

Fig. 2 (a) Fluid influx problem. (b) Maximum slip velocity on the fault as a function of time for simulations with three different state evolution distances, d_c, and nucleation lengths. Unstable slip / earthquakes occur for $d_c = 10$ and 40 μm, whereas aseismic, slow slip occurs for $d_c = 80$ μm. (c) Final slip is nearly identical in all cases. Compare the relatively steady accumulation of slip for $d_c = 80$ μm in (c), where slip contours are plotted every 2000 time steps, with the rapidly accumulating slip for $d_c = 10$ and 40 μm, shown in (d) as slip contours every 20 time steps when slip velocity $V > 1$ mm/s. Aseismic slip preceding instability is confined to approximately 1 m for $d_c = 10$ μm and 3 m for $d_c = 40$ μm.

is the hydraulic diffusivity. The decrease in effective normal stress reduces fault strength (Eq. 107) and causes slip velocity to increase. Slip increases on the fault, initially quite slowly and in a stable, aseismic manner.

This initial slip is confined to a nucleation region scaling approximately with the critical length scale h_f (Eq. 112). From Figure 2d, we identify the nucleation length as approximately 1 m for $d_c = 10$ μm and 3 m for $d_c = 40$ μm. For both of those cases, the nucleation length is less than the fault length (4 m), so slip accelerates to instability. For $d_c = 80$ μm, the nucleation length is larger than the fault length, so slip never becomes unstable.

The evolution of slip velocity during an earthquake is shown in Figure 4b. Slip localizes in the late stages of nucleation, and then the earthquake begins. Characteristic of an expanding shear crack, slip velocity is peaked at the two rupture fronts (i.e., crack tips), which propagate outward from the nucleation zone. Rupture arrests soon after reaching the tips of the fault.

In a poroelastic solid, changes in mean stress are coupled to changes in pore pressure. Because slip is right-lateral, the material surrounding the right rupture

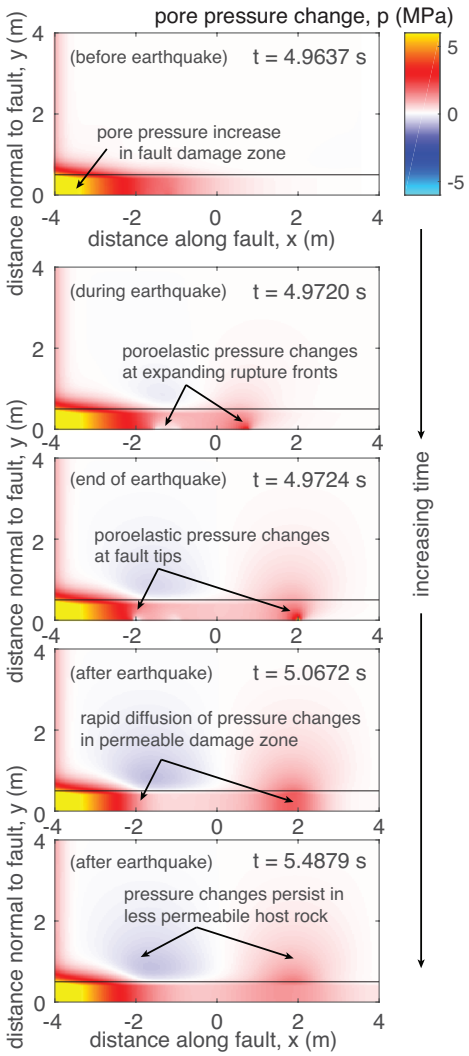

Fig. 3 Snapshots of change in pore pressure immediately before, during, at the end, and after an earthquake. A constant pressure gradient on the left side drives fluid into the domain, primarily through the high permeability fault damage zone. An earthquake is triggered by reduction of effective normal stress and hence fault strength. Changes in mean stress and pore pressure accompany fault slip, and are especially pronounced at the rupture fronts and fault tips. The pore pressure changes in the damage zone diffuse rapidly, while pressure equilibration from Darcy flow in the less permeable host rock is more gradual. Shown for $d_c = 10$ μm simulation.

front is put into compression, causing an effectively undrained pressure increase (Figure 3) and reduction of effective normal stress (Figure 4a) and fault strength. Suction occurs at the left rupture front, further clamping the fault and increasing fault strength. This poroelastic effect, identified in previous studies [38,11], as well as asymmetry from fluid injection, favors rupture propagation to the right. After

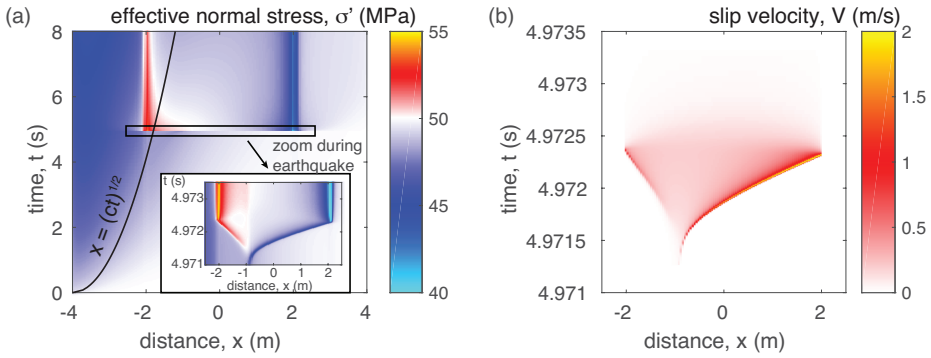

Fig. 4 (a) Space-time plot of effective normal stress on the fault; inset shows evolution during the earthquake. The curve $x = \sqrt{ct}$ shows diffusion of pore pressure through the fault damage zone with hydraulic diffusivity c. The reduction in effective stress triggers the earthquake; strains accompanying fault slip, especially at the rupture fronts, further change pore pressure through poroelastic coupling. (b) Space-time plot of slip velocity during the earthquake, showing maximum slip velocity at the expanding rupture fronts. Both shown for $d_c = 10$ μm simulation.

the rupture arrests, the stress and pore pressure concentrations at the tips of the fault decreases in response to fluid diffusion (Figure 3).

We remark here that fault slip facilitates and enhances the advance of pore pressure changes along the fault. The reduction in effective stress after slip has occurred extends well beyond the predicted diffusion length (Figure 4a). While illustrated here for a fault experiencing unstable slip, the same behavior is seen for the simulation involving stable, aseismic slip. This suggests the intriguing possibility that poroelastic coupling between slip, solid deformation, and fluid diffusion can enhance the penetration of pore pressure changes along fault zones. A similar phenomenon was recently pointed out by Viesca [48].

13 Conclusion

We have introduced an SBP-SAT finite difference method for the linear poroelastic equations in two equivalent formulations. Using the energy method, we established well-posedness and semi-discrete stability. The correctness of the schemes were verified through rigorous convergence studies using the method of manufactured solutions and Mandel's problem, for which the expected convergence rates for second and fourth order SBP operators were obtained. The method was then extended to handle fault dynamics using rate-and-state friction.

We then simulated earthquakes and slow slip events triggered by fluid injection, pointing out how slight differences in frictional properties can control the stability of slip. Phenomena unique to the fully coupled poroelastic problem are emphasized, such as poroelastic changes in effective normal stress at the propagating rupture fronts and subsequent diffusive equilibration of pressure following slip events. The simulations demonstrate how fault slip can facilitate the transmission of pore pressure changes along faults, beyond that expected from a purely diffusive process. Future work exploring the implications of this observation could be conducted using the simulation procedure we have introduced.

From a numerical perspective, suggestions for future work include extending the scheme to three spatial dimensions with curvilinear coordinates, imposing Dirichlet conditions directly instead of as Robin conditions, and generalizing the implementation to modeling the fault as an interface instead of as a boundary.

Acknowledgements This work was supported by the Stanford Consortium for Induced and Triggered Seismicity and by a scholarship to K.T. and V.S. from the Anna Whitlocks minnesfond. Discussions with Ossian O'Reilly on numerical methods and assistance from Kali Allison on the PETSc implementation are gratefully acknowledged.

References

1. Aagaard, B.T., Knepley, M.G., Williams, C.A.: A domain decomposition approach to implementing fault slip in finite-element models of quasi-static and dynamic crustal deformation. J. Geophys. Res. **118**(6), 3059–3079 (2013)
2. Abousleiman, Y., Cheng, A.D., Cui, L., Detournay, E., Roegiers, J.C.: Mandel's problem revisited. Geotechnique **46**(2), 187–195 (1996)
3. Atkinson, G.M., Eaton, D.W., Ghofrani, H., Walker, D., Cheadle, B., Schultz, R., Shcherbakov, R., Tiampo, K., Gu, J., Harrington, R.M., Liu, Y., van der Baan, M., Kao, H.: Hydraulic fracturing and seismicity in the Western Canada sedimentary basin. Seismol. Res. Lett. **87**(3), 631–647 (2016)
4. Biot, M.A.: General theory of three-dimensional consolidation. J. Appl. Phys. **12**(2), 155–164 (1941)
5. Cheng, A.H.D., Detournay, E.: A direct boundary element method for plane strain poroelasticity. Int. J. Numer. Anal. Met. **12**, 551–572 (1988)
6. Dean, R.H., Gai, X., Stone, C.M., Minkoff, S.E.: A comparison of techniques for coupling porous flow and geomechanics. SPE Journal **11**(01), 132–140 (2006)
7. Deichmann, N., Giardini, D.: Earthquakes induced by the stimulation of an enhanced geothermal system below Basel (Switzerland). Seismol. Res. Lett. **80**(5), 784–798 (2009)
8. Deng, K., Liu, Y., Harrington, R.M.: Poroelastic stress triggering of the December 2013 Crooked Lake, Alberta, induced seismicity sequence. Geophys. Res. Lett. **43**(16), 8482–8491 (2016)
9. Detournay, E., Cheng, A.H.D.: Fundamental of poroelasticity, Ch. 5 in Comprehensive Rock Engineering, Vol. 2, Editor, C. Fairhurst (1993)
10. Dieterich, J.H., Richards-Dinger, K.B., Kroll, K.A.: Modeling injection-induced seismicity with the physics-based earthquake simulator RSQSim. Seismol. Res. Lett. **86**(4), 1102–1109 (2015)
11. Dunham, E.M., Rice, J.R.: Earthquake slip between dissimilar poroelastic materials. J. Geophys. Res. **113**(B9) (2008)
12. Ellsworth, W.L.: Injection-induced earthquakes. Science **341**(6142), 1225,942 (2013)
13. Erickson, B.A., Dunham, E.M.: An efficient numerical method for earthquake cycles in heterogeneous media: Alternating subbasin and surface-rupturing events on faults crossing a sedimentary basin. J. Geophys. Res. **119**(4), 3290–3316 (2014)
14. Hairer, E., Norsett, S.P., Wanner, G.: Solving Ordinary Differential Equations I: Nonstiff Problems. Springer-Verlag (1993)
15. Hairer, E., Wanner, G.: Solving Ordinary Differential Equations II: Stiff and Differential-Algebraic Problems. Springer-Verlag (1996)
16. Hetland, E., Simons, M., Dunham, E.: Post-seismic and interseismic fault creep i: model description. Geophys. J. Int. **181**(1), 81–98 (2010)
17. Jha, B., Juanes, R.: Coupled multiphase flow and poromechanics: A computational model of pore pressure effects on fault slip and earthquake triggering. Water Resour. Res. **50**(5), 3776–3808 (2014)
18. Keranen, K.M., Weingarten, M., Abers, G.A., Bekins, B.A., Ge, S.: Sharp increase in central Oklahoma seismicity since 2008 induced by massive wastewater injection. Science **345**(6195), 448–451 (2014)
19. Kim, J., Tchelepi, H., Juanes, R.: Stability and convergence of sequential methods for coupled flow and geomechanics: Fixed-stress and fixed-strain splits. Comput. Method. Appl. M. **200**(13), 1591–1606 (2011)

20. Kozdon, J.E., Dunham, E.M., Nordström, J.: Interaction of waves with frictional interfaces using summation-by-parts difference operators: Weak enforcement of nonlinear boundary conditions. J. Sci. Comput. **50**(2), 341–367 (2012)
21. Lapusta, N., Rice, J.R., Ben-Zion, Y., Zheng, G.: Elastodynamic analysis for slow tectonic loading with spontaneous rupture episodes on faults with rate-and state-dependent friction. J. Geophys. Res. **105**(B10), 23,765–23,789 (2000)
22. Marone, C.: Laboratory-derived friction laws and their application to seismic faulting. Annu. Rev. Earth Pl. Sc. **26**(1), 643–696 (1998)
23. Mattsson, K.: Summation by parts operators for finite difference approximations of second-derivatives with variable coefficients. J. Sci. Comput. **51**(3), 650–682 (2012)
24. Mattsson, K., Ham, F., Iaccarino, G.: Stable boundary treatment for the wave equation on second-order form. J. Sci. Comput. **41**(3), 366–383 (2009)
25. Mattsson, K., Nordström, J.: Summation by parts operators for finite difference approximations of second derivatives. J. Comput. Phys. **199**(2), 503–540 (2004)
26. Mattsson, K., Svärd, M., Shoeybi, M.: Stable and accurate schemes for the compressible navier–stokes equations. J. Comput. Phys. **227**(4), 2293–2316 (2008)
27. McClure, M.W., Horne, R.N.: Investigation of injection-induced seismicity using a coupled fluid flow and rate/state friction model. Geophys. **76**(6), WC181–WC198 (2011)
28. Meng, C.: Benchmarking Defmod, an open source fem code for modeling episodic fault rupture. Comput. Geosci. **100**, 10–26 (2017)
29. Miah, M., Martín, L.B., Foxall, W., Rutqvist, J., Rinaldi, A.P., Mullen, C.: Development of a hydro-geomechanical model to simulate coupled fluid flow and reservoir geomechanics. In: Proceedings of the TOUGH Symposium (2015)
30. Mikelić, A., Wheeler, M.F.: Convergence of iterative coupling for coupled flow and geomechanics. Comput. Geosci. **17**(3), 455–461 (2013)
31. Minkoff, S.E., Stone, C.M., Bryant, S., Peszynska, M., Wheeler, M.F.: Coupled fluid flow and geomechanical deformation modeling. J. Petrol. Sci. Eng. **38**(1), 37–56 (2003)
32. Preisig, M., Prévost, J.H.: Stabilization procedures in coupled poromechanics problems: A critical assessment. Int. J. Numer. Anal. Met. **35**(11), 1207–1225 (2011)
33. Rice, J.R.: Spatio-temporal complexity of slip on a fault. J. Geophys. Res. **98**(B6), 9885–9907 (1993)
34. Rice, J.R., Cleary, M.P.: Some basic stress diffusion solutions for fluid-saturated elastic porous media with compressible constituents. Rev. Geophys. **14**(2), 227–241 (1976)
35. Rice, J.R., Lapusta, N., Ranjith, K.: Rate and state dependent friction and the stability of sliding between elastically deformable solids. J. Mech. Phys. Solids **49**(9), 1865–1898 (2001)
36. Rice, J.R., Ruina, A.L.: Stability of steady frictional slipping. J. Appl. Mech. **50**(2), 343–349 (1983)
37. Roache, P.J.: Verification and validation in computational science and engineering. Hermosa (1998)
38. Rudnicki, J.W., Rice, J.R.: Effective normal stress alteration due to pore pressure changes induced by dynamic slip propagation on a plane between dissimilar materials. J. Geophys. Res. **111**(B10) (2006)
39. Ruina, A.: Slip instability and state variable friction laws. J. Geophys. Res. **88**(B12), 10,359–10,370 (1983)
40. Segall, P.: Earthquakes triggered by fluid extraction. Geology **17**(10), 942 (1989)
41. Segall, P., Lu, S.: Injection-induced seismicity: Poroelastic and earthquake nucleation effects. J. Geophys. Res. **120**(7), 5082–5103 (2015)
42. Selvadurai, A.P.: Mechanics of poroelastic media. Springer Science & Business Media (2013)
43. Strand, B.: Summation by parts for finite difference approximations for d/dx. J. Comput. Phys. **110**(1), 47–67 (1994)
44. Svärd, M., Nordström, J.: Review of summation-by-parts schemes for initial–boundary-value problems. J. Comput. Phys. **268**, 17–38 (2014)
45. Torberntsson, K., Stiernström, V.: A high order finite difference method for simulating earthquake sequences in a poroelastic medium. Tech. rep., Uppsala University (2016)
46. van Thienen-Visser, K., Breunese, J.: Induced seismicity of the Groningen gas field: History and recent developments. The Leading Edge **34**(6), 664–671 (2015)
47. Verruijt, A.: Theory and problems of poroelasticity. Delft University of Technology (2013)
48. Viesca, R.: Elastic stress transfer as a diffusive process due to aseismic fault slip in response to fluid injection. Abstract MR41E-02 presented at 2015 Fall Meeting, AGU, San Francisco, Calif., 14–18 Dec. (2015)

49. Wang, H.: Theory of Linear Poroelasticity with Applications to Geomechanics and Hydrogeology. Princeton University Press (2000)
50. White, J.A., Borja, R.I.: Stabilized low-order finite elements for coupled solid-deformation/fluid-diffusion and their application to fault zone transients. Comput. Method. Appl. M. **197**(49), 4353–4366 (2008)
51. White, J.A., Borja, R.I.: Block-preconditioned Newton–Krylov solvers for fully coupled flow and geomechanics. Comput. Geosci. **15**(4), 647–659 (2011)